

CHAPTER 4. NUMERICAL MODELING ANALYSIS OF CSL IN DRILLED SHAFTS

Many factors influence the sonic wave velocity and energy in a drilled shaft, such as structural defects, tube bending, tube debonding, and sensor orientation. In this chapter, numerical modeling analysis will be used to evaluate major factors resulting in CSL velocity and energy variations.

4.1 Geostructural Analysis Package (GAP) Model Description

The numerical modeling studies performed in the remainder of this study use the Geostructural Analysis Package (GAP). This method combines well-developed techniques from Discrete Element Method (DEM), Particle Flow Code (PFC), Material Point Method (MPM), and Finite Difference (FD) methods, resulting in efficient simulation of high-resolution dynamic modeling applications. Figure 4.1 shows the material color palettes used in the GAP models. These palettes are used to display various properties, such as velocity, wave compression, average stress, temperature, heat generation, hydration phase, tension strength, modulus, damping, etc. Defects, such as honeycombs, cracking, and debonding, are shown in a graduated red palette. Darker colors on the left represent lower property values. The ranges for each property used in subsequent models, corresponding to material color palettes, are shown in Table 4.1.

The right of Figure 4.1 shows the drilled shaft used in subsequent numerical models. A 1 m reinforced shaft (4.5 m long) is in the center, surrounded by dry sand in the top meter, wet sand in the next meter, two meters of clay, and one meter of rock at the base. The shaft is socketed one half meter in the rock. Portions of the model are hidden for internal viewing. Half of the wet sand and clay are hidden to show the location of the shaft. The concrete in the shaft is hidden from a depth of 1 to 2.5 m, to show the internal rebar, access tubes, and support cage.

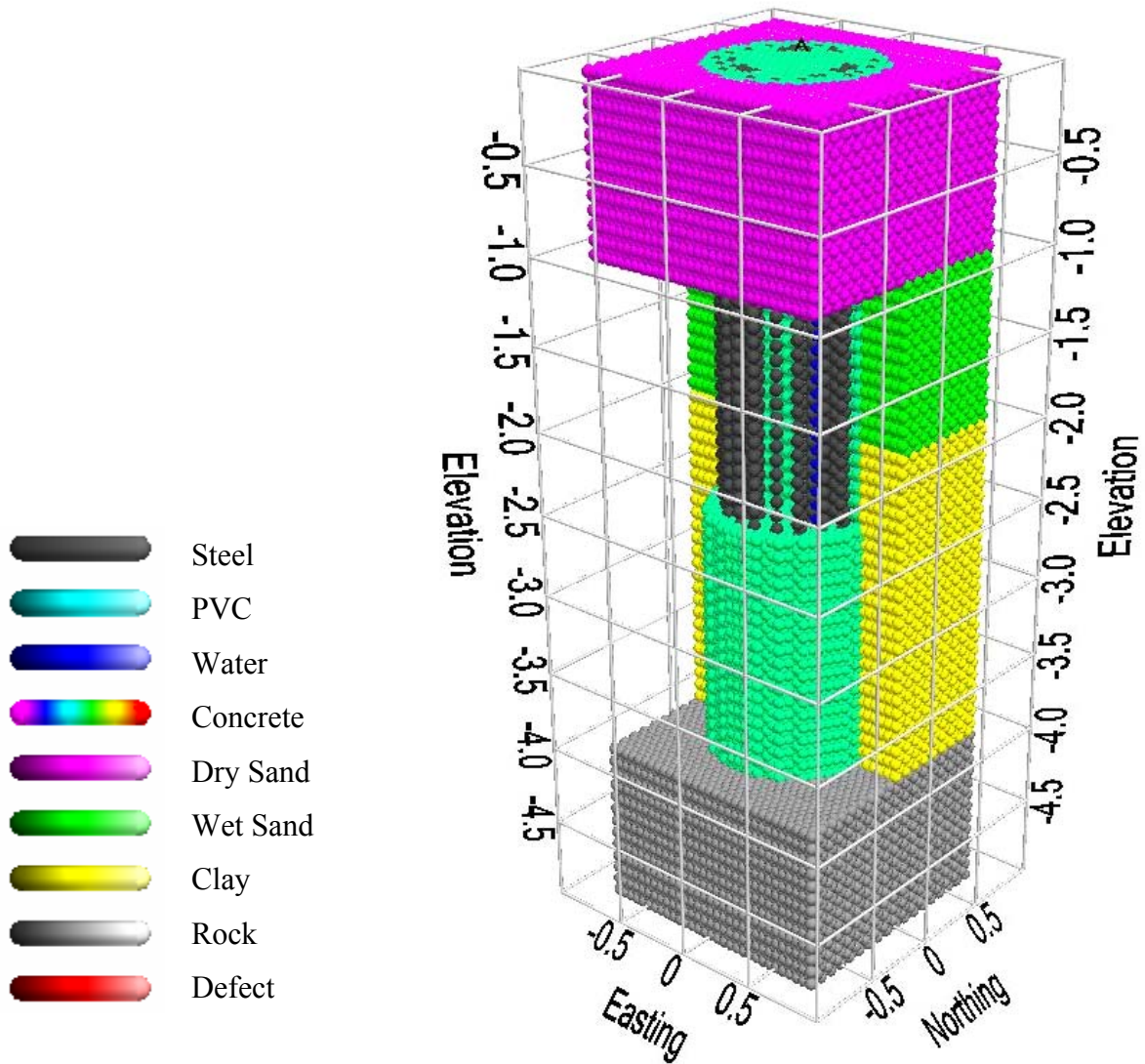


Figure 4.1. Plot. Material Palettes used in GAP Models. Defects Shown in Red Include Honeycombs, Cracking, and Debonding. Darker Colors on the Left Represent Lower Values. These Palettes are used to Display Corresponding Velocity, Wave Compression, Average Stress, Temperature, Heat Generation, Hydration Phase, Tension Strength, Modulus, etc. A Cross-section of the 1 m Drilled Shaft used in the Study is Shown on the Right. The Shaft is in the Center, Surrounded by Dry Sand, Wet Sand, Clay, and Rock. Portions of the Wet Sand, Clay, and Concrete are Hidden to Show the Internals of the Model.

Table 4.1 Property Ranges Corresponding to Material Color Palettes

Property	Minimum	Maximum
Cracking	-25%	25%
Change in Cracking	-25%	25%
Compression Stress Loading (N)	-0.001	0.001
Change in Compression Stress Loading (N)	-0.001	0.001
Temperature (°C)	10	50
Change in Temperature (°C)	-10	10
Hydration	0%	100%
Change in Hydration	-15%	15%
Curing Compression (N)	-1.0 x10 ⁻⁴	1.0 x10 ⁻⁴
Change in Curing Compression (N)	-1.00x10 ⁻⁴	1.0 x10 ⁻⁴
Heat (Cal)	0	0.001
Change in heat (Cal)	-0.001	0.001
Seismic Compression (N)	-1.0x10 ⁻¹⁰	1.0 x10 ⁻¹⁰
Change in Seismic Compression (N)	-1.0 x10 ⁻¹⁰	1.0 x10 ⁻¹⁰

Table 4.2 Material Properties used in Models

Material	Tension Strength N/m ²	Specific Gravity	Pwave Velocity (m/s)	Coefficient of Restitution	Percent Cracked	Percent Void	Void Material	Thermal Conductivity
Steel	10000	7.85	8000	0.9	0	0		0.99
PVC	50	1.5	1000	0.9	0	0		0.5
Water	1	1	1500	0.9	0	0		0.25
Concrete	150	4	4000	0.3	0	0		0.5
Dry Sand	1	2	400	0.1	90	2		0.6
Wet Sand	50	2.5	600	0.2	30	2	Water	0.7
Clay	100	3	2000	0.2	5	0		0.8
Rock	5000	4	7000	0.4	0	0		0.4
Honeycomb	50	2	3200	0.2	10	20		0.8
Debonding	0	2	10	0.2	90	90		0.8
Cracking	50	4	4000	0.3	90	0		0.5
Void	0	0	0	0	0	100		0

Figure 4.2 shows the location of a sample 2-D slice in the drilled shaft model. Slices may be extracted at different depths depending on surrounding ground conditions, but Figure 4.2 applies to most of the 2-D models throughout this study. The resolution of the 2-D models is 1 cm, meaning that each spherical model element is 1 cm in diameter.

The three access tubes are numbered clockwise, starting from the tube at the top. Access tube #1 is at the top (north), tube #2 is in the lower right (south east), and tube #3 is in the lower left (south west). The access tube material is steel, except for the 3-D model comparing PVC with steel. The tubes are filled with water. The inside tube diameter is 50 mm. The access tubes are 320 mm from the center of the shaft.

The steel rebar cage is represented by 20 rebar distributed around the perimeter, each 50 mm in diameter. The cage diameter is 0.8 m. The rebar is 10 cm in diameter, distributed in three pairs inside the rebar cage. Steel is used for the rebar.

Figure 4.3 shows the location of a sample 3-D section in the drilled shaft model. The resolution of the 3-D CSL models in this chapter, for tube material and tube debonding, is 20 mm. Top portions of the 3-D models are hidden for display purposes. Compression waves are shown in the hidden portions for positive compression values, to show wave propagation in 3-D.

4.2 Factors Affecting CSL Velocity Measurements

Typically, the wave velocity of concrete in a drilled shaft is estimated from the first arrival time obtained during CSL measurements, using the separation distance between the source and receiver tubes at the top of the shaft, assuming the tubes remain vertical throughout the shaft. The first arrival time may correspond to the point at which the signal amplitude first fluctuates, or at the first peak or trough identifiable in the waveform. Uncertainties in source and receiver locations and variations in the definition of the first arrival must be taken into account when interpreting CSL data. Very small changes in source/receiver separation distance and the selection of the first arrival time, called the arrival pick, can result in large velocity variations. Without proper tube bending measurements, sensor alignment, or proper waveform analysis for first arrival determination, CSL data should be used as a relative guide rather than an absolute value.

Tube locations below the top of the shaft are unknown and are typically assumed parallel. The tube distances at the top of the shaft are occasionally adjusted during the CSL data analysis to obtain a tube separation resulting in more “reasonable” velocities. Tube bending near the top of the shaft is common and often used to justify the practice of adjusting arrival picks in this fashion. This practice can introduce apparent velocity variations in good concrete, or remove velocity variations in defective concrete.

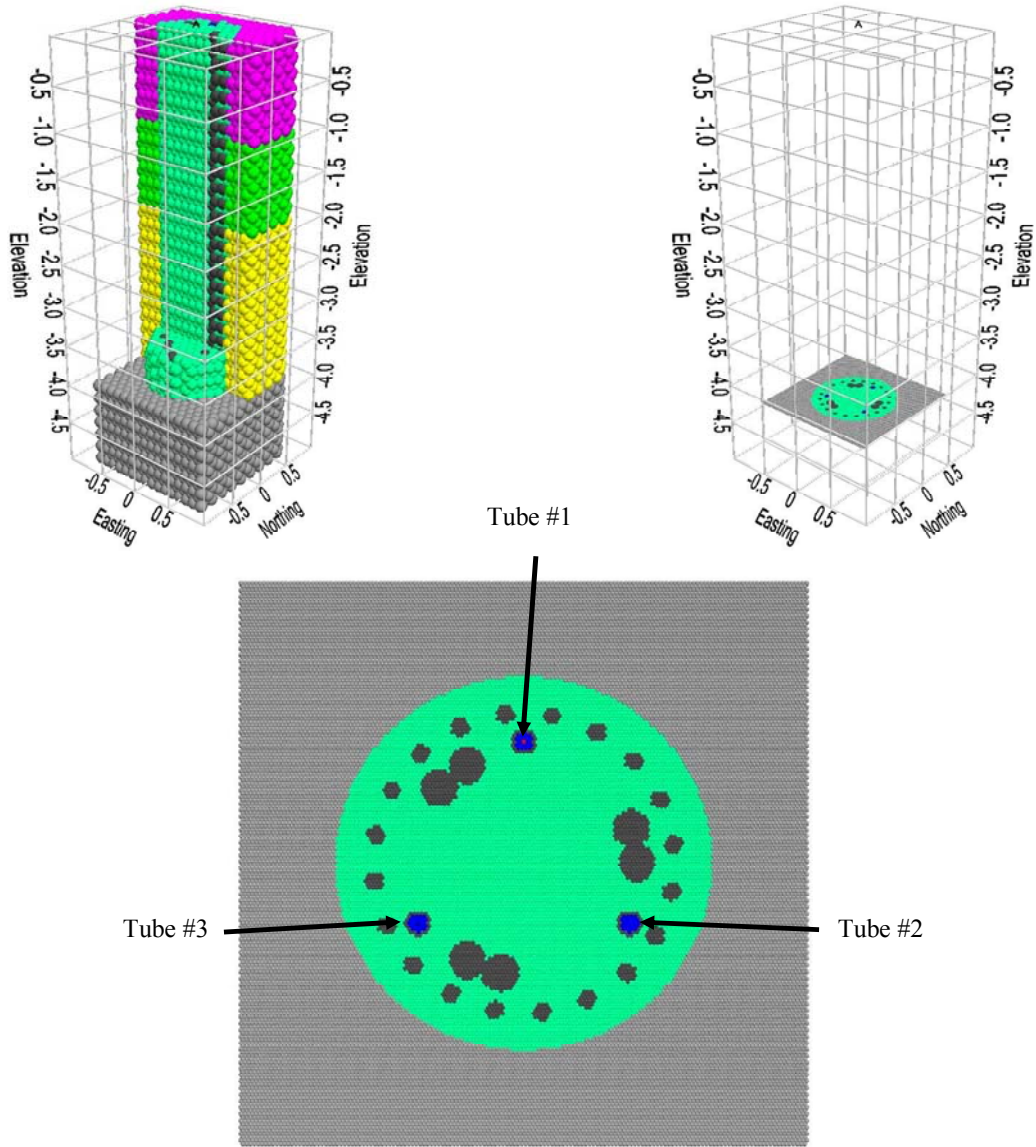


Figure 4.2. Plot. Location of Drilled Shaft Cross-section Surrounded by Rock

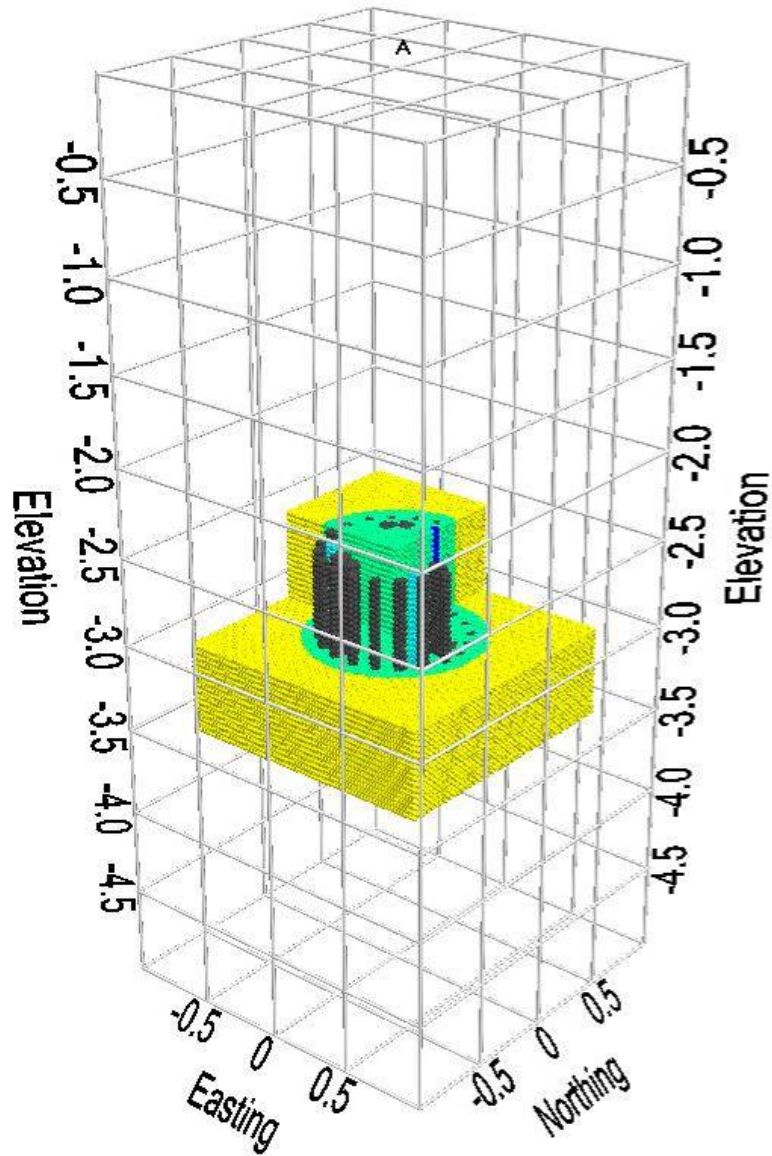


Figure 4.3. Plot. Location of 3D Section within Drilled Shaft

Plots of the signal energy versus depth are often generated in CSL surveys, in addition to plots of first arrival picks. The definition of signal energy often varies from system to system. The signal energy may be determined by summing up the absolute values of a set number of signal samples after the first arrival time, or may be measured from the first major peak after the first arrival, or from the maximum signal amplitude. The energy and velocity plots versus depth are generally used together to indicate regions of compromised concrete quality. Some CSL data collection systems do not attempt to analyze the signal data, but simply plot the waveforms with depth for visual inspection.

CSL velocity variations may indicate zones of lower quality concrete, voids, and honeycombs in a drilled shaft. Actual defects are difficult to detect using CSL data in its present form, because CSL measurements must be assumed accurate and absolute, not approximate, relative, and massaged. When good CSL data is available and reconstructed variations can be trusted as defects, the influence of a defect on foundation performance should be carefully examined. A drilled shaft should not be rejected simply because certain zones suggest a lower concrete quality. Design loads and the load bearing assessment should be taken into consideration relative to the anomaly location within the drilled shaft. For example, an anomaly near the base of a friction shaft may not significantly affect the load carrying capacity. The same anomaly in an end-bearing shaft in very loose soil may be of greater concern, depending on how the loads are applied to the shaft and transferred to the surrounding soil. An end bearing shaft experiences friction with the surrounding ground, as does a friction shaft. Actual loading conditions and load distribution should be evaluated to determine the effect of anomalies on overall shaft performance for defect definition.

CSL is not restricted by shaft length and can detect multiple anomalies within a drilled shaft, with accurate data collection. Combined with tomography and the option to create more signals on angled or offset paths, the size and location of defects can be better estimated. However, CSL is relatively expensive and requires pre-installation of access tubes. Debonding between tubes and concrete can seriously affect the results, corrupting measurements of entire sections of the shaft. Variations in hydration rates during concrete curing can also create anomalies in first arrival times and signal energies, falsely indicating lower quality concrete.

If only first arrival times or signal energy levels are used, no information outside the rebar cage can be obtained from CSL tests. Placing the access tubes outside the reinforcing cage significantly reduces the quality of data and complicates interpretation. Signals attenuate due to thermal cracking and debonding of the concrete in regions adjacent to the rebar cage. In friction shafts, concrete integrity outside the steel-reinforcement cage is more critical to assess than the core of the shaft. This is a serious limitation of the CSL test.

4.3 CSL Velocity Variations

Actual variations in sonic velocity within concrete structures such as drilled shafts originate from two sources, “structural” and “chemical”. This division breaks down naturally from the basic nature of concrete structures. Fundamentally concrete structures can be conceptualized as a form of artificial stone, formed from constituent components as a result of a clearly defined chemical process - the hydration of the cement. Water chemically reacts with the cement in the hydration

process. The cement paste does not dry out, and water does not escape into surrounding porous materials or evaporate into the air, as is commonly thought. Defects resulting in a substantial reduction in the strength of concrete structures from its designed capacity may have two origins. Structural defects can be the result of a physical deviation in the process of forming the concrete structure, since structural design assumes a uniform mass of well mixed concrete. Defects may also occur when the concrete mixture is placed in the desired form as intended. These defects come from inherent weakness and variability in the process of the concrete curing itself. From the time concrete is placed to the time it is fully set, many dynamic processes take place. Variations in chemical reactions that form the concrete can result in decreased design strength. A defect in the concrete that decrease the performance of the shaft can be classified as a structural defect.

4.4 Effect of Surrounding Material on CSL Signals

Figures 4.4 – 4.9 compare CSL signals from a drilled shaft surrounded by rock with signals from a shaft surrounded by clay. The full waveforms are shown for each model for comparison, since precise definitions of arrival times and energies are not standardized and difficult at times to quantify. The waveforms for the rock/clay model are shown in Figure 4.9.

Figure 4.4 shows the compression wave propagating from the top access tube (Tube #1) after 20 μ s. The surrounding rock is displayed on the left with a gray palette, and the shaft in soil is on the right with a yellow palette. The difference is shown at the bottom, but there is no difference between the compression waves at this stage.

The cross-section shows three water-filled steel access tubes with an impulse source located in the top tube (Tube #1), and receivers located in the center of the two lower tubes (Tubes #2 and #3).

Figure 4.5 shows the compression wave at 60 μ s, as the wave first interacts with the surrounding ground. The difference plot shows the reflection, with the same polarity as the source signal. The rock has a higher stiffness than the clay, resulting in a reflection with the same polarity.

The compression wave continues to propagate to the edge of the shaft and encounters the surrounding soil. A portion of the wave propagates into the soil, while another portion reflects back into the concrete shaft. The concrete has a higher stiffness and density than the clay, resulting in a reverse-polarity reflection. However, the rock has higher stiffness than concrete, so results in a reflection with the same polarity.

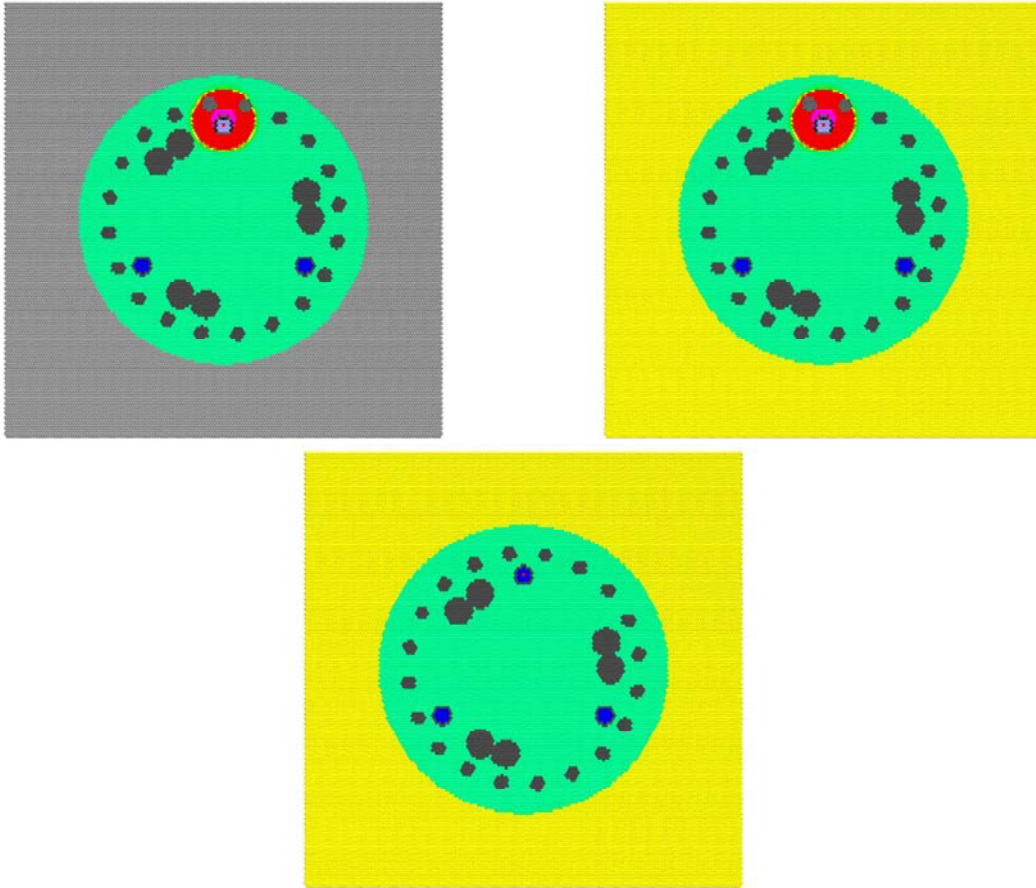


Figure 4.4. Plot. Rock (Top Left) vs. Clay (Top Right) at 20 μ s, with Difference (Bottom)

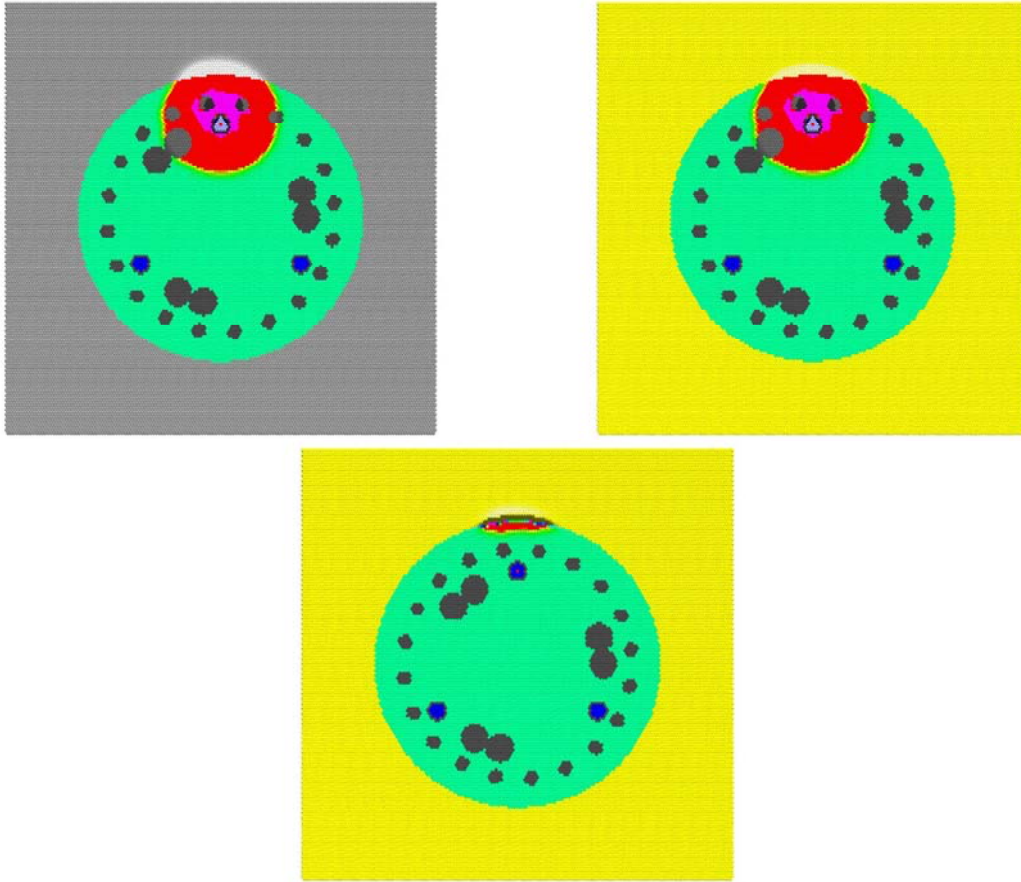


Figure 4.5. Plot. Rock (Top Left) vs. Clay (Top Right) at 60 μ s, with Difference (Bottom)

Figure 4.6 shows the compression wave at $120 \mu\text{s}$, as the first tension wave interacts with the surrounding ground. The compression wave travels faster through the rock than through the clay, because of the higher stiffness of the rock. The difference plot shows the reflection bending around the perimeter of the shaft, corresponding to the interaction of the wavefront with the surrounding ground.

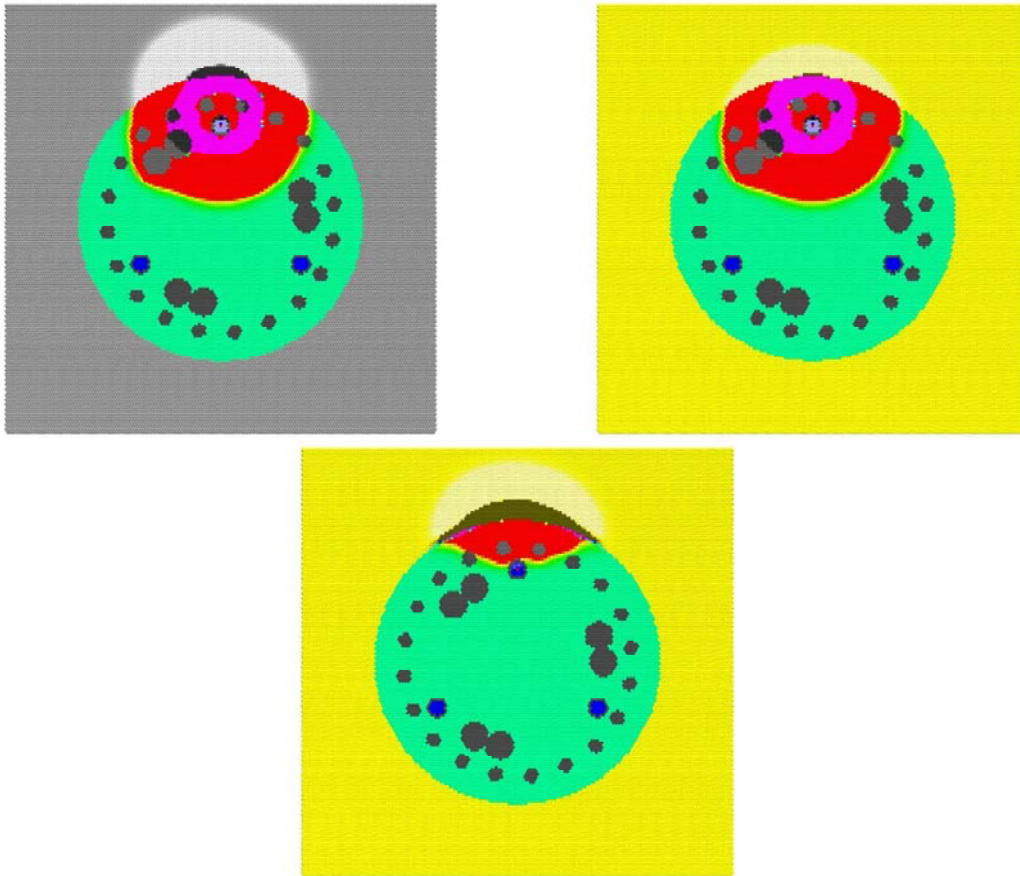


Figure 4.6. Plot. Rock (Top Left) vs. Clay (Top Right) at $120 \mu\text{s}$, with Difference (Bottom)

Figure 4.7 shows the compression wave at $300 \mu\text{s}$, as the first compression wave reaches the access tubes. The arrival is identical for both access tubes. The difference plot shows the reflection lagging far behind, contributing no effect on the initial waveform.

The sensors in the access tubes measure the compression waves in the water, which may not necessarily correspond to the compression waves in the concrete. Compression in the water is indicated using a gradient blue palette, with lighter blue for positive compression, blue for neutral compression, and dark blue for negative compression, or tension.

The compression wave propagates through the drilled shaft, followed by a tension wave. The wavefront is circular when traveling through a homogenous medium.

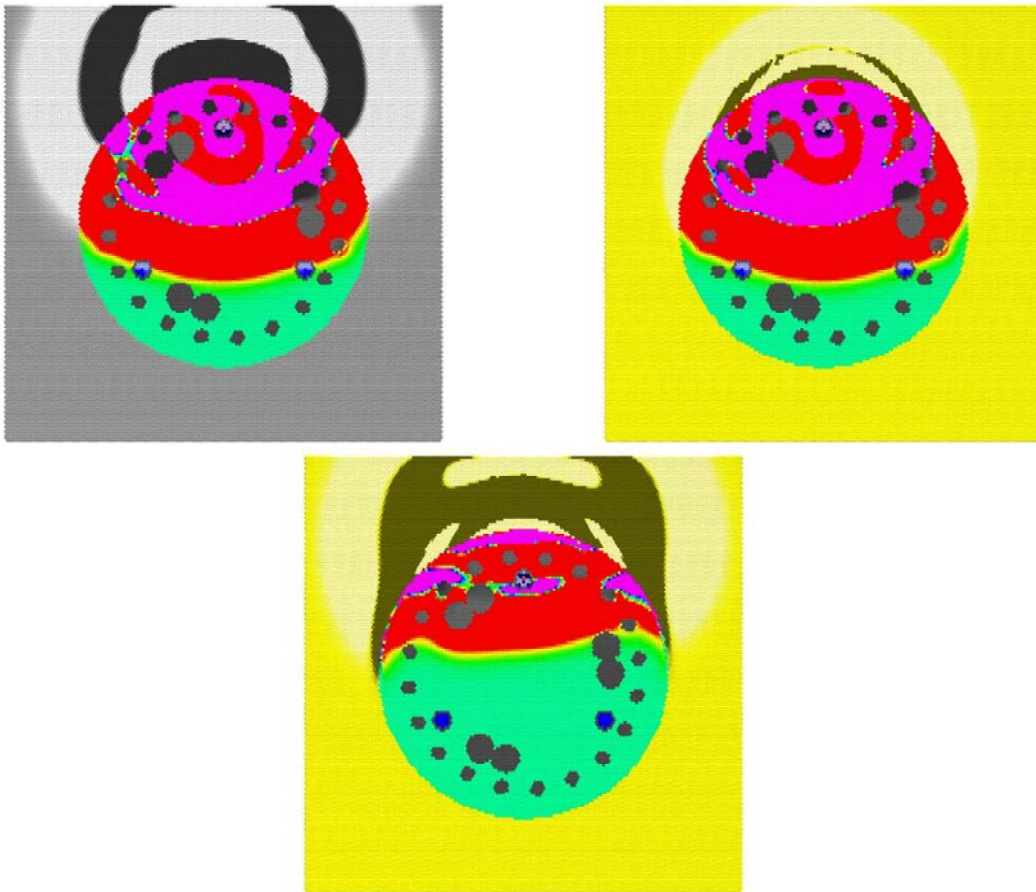


Figure 4.7. Plot. Rock (Top Left) vs. Clay (Top Right) at $300 \mu\text{s}$, with Difference (Bottom)

Figure 4.8 shows the compression wave at 500 μs , as the first tension wave reaches the access tubes. This also happens to correspond to the instant when the concrete/ground reflection first reaches the access tubes. The tension wave in the water is lagging behind the tension wave in the concrete.

The compression wave patterns in the access tubes should be noted. The compression wave in the receiver access tube exhibits a slightly delayed arrival due to the lower compression wave velocity of water. As the compression wave first contacts the tube, the wave travels quickly around the tube due to the higher compression wave velocity of steel. However, the water in the tube has a significantly lower compression wave velocity, resulting in a slight delay in arrival time measurements.

The compression waves in the source tube do not necessarily correspond to the compression waves propagating through the concrete due to multiple reflections among the water, steel tube, and concrete interfaces.

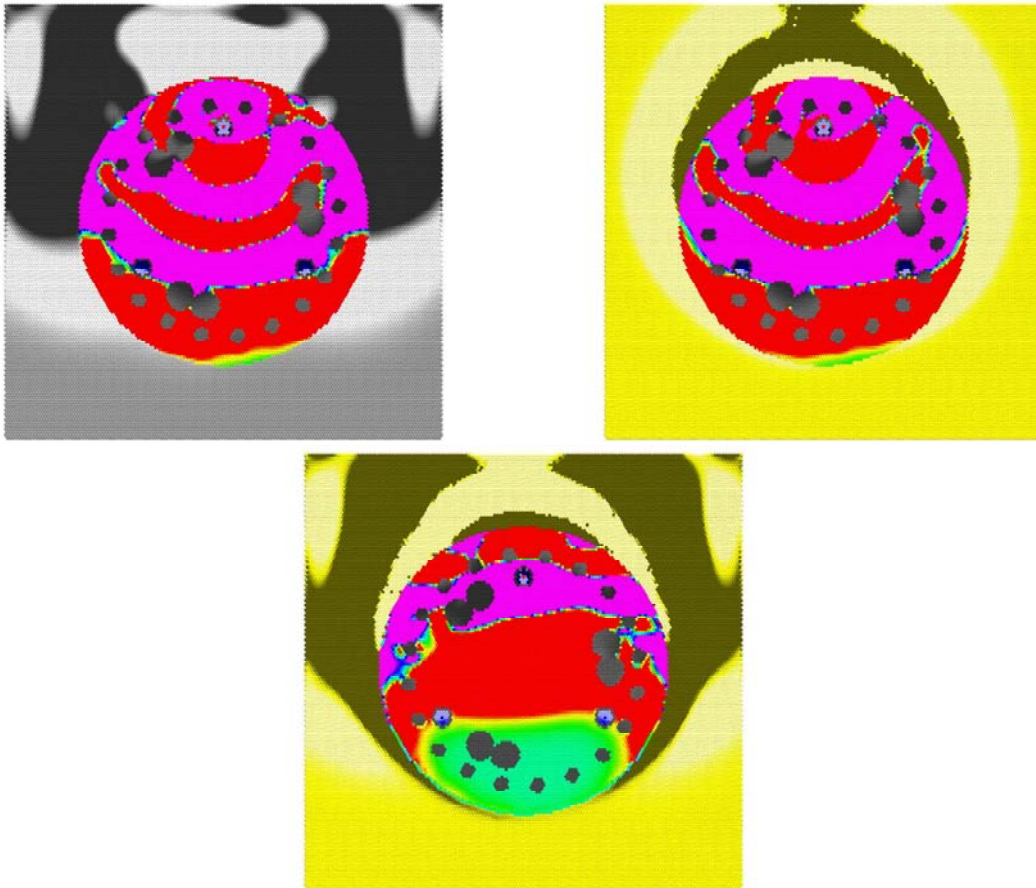


Figure 4.8. Plot. Rock (Top Left) vs. Clay (Top Right) at 500 μs , with Difference (Bottom)

Figure 4.9 compares the waveforms collected in the access tubes. The waveform in the top graph refers to the signal collected in the shaft surrounded by rock and clay, with the source in access tube #1, and the receiver in tube #2. The x-axis is plotted in milliseconds, and the y-axis is average compression force, in nano-Newtons. The difference between the rock and clay surrounded shafts is also shown in the plot. Similarly, the waveforms collected in access tube #3 are shown in the lower graph.

Since the rock has only a slightly higher density and stiffness than concrete, the reflected compression arrival has slightly higher amplitude than the soil reflection. This study is primarily concerned with the first arrival, as velocity determination using CSL uses only first arrival information. This example indicates that important information about the shaft outside of the reinforcement cage and the environment surrounding the shaft is contained in the full waveform, and can be extracted using model inversion techniques.

The surrounding environment can have a large effect on first arrivals during the curing phase. Since initial CSL measurements are acquired during and shortly after the second hydration phases of concrete curing, this is an important factor to take into consideration. The effects of the surrounding environment on concrete temperature and CSL velocity are presented later in this study.

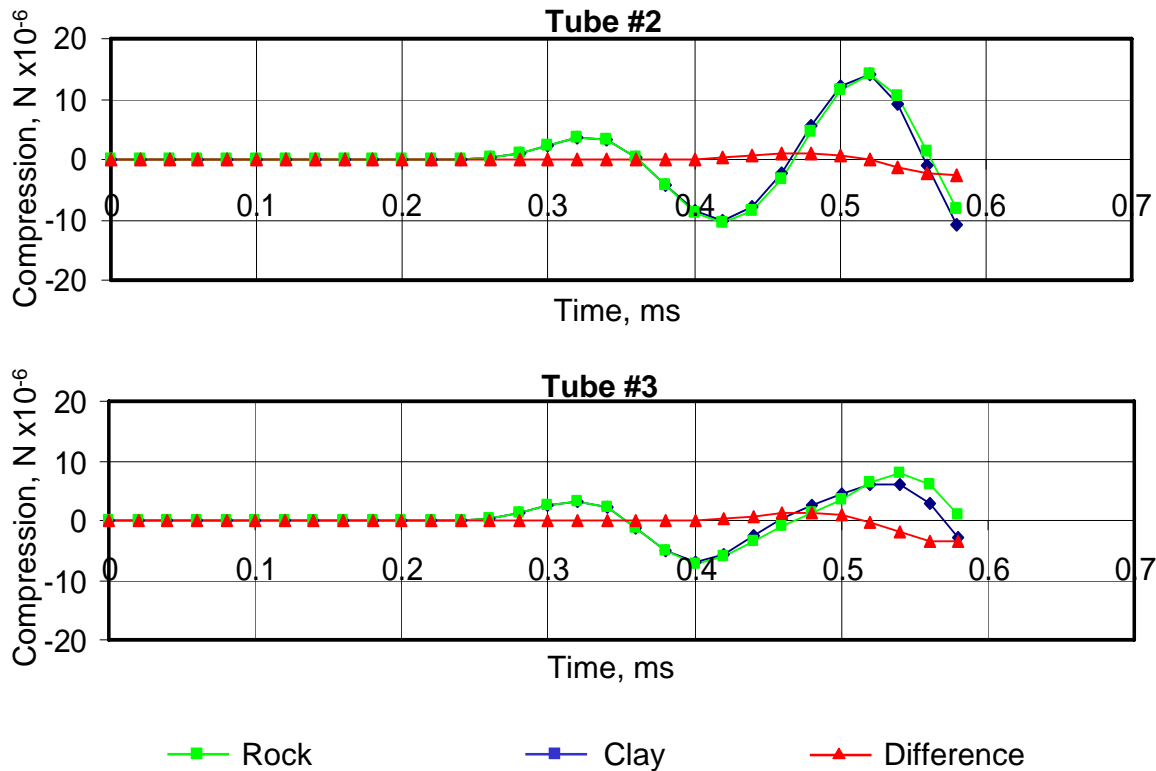


Figure 4.9. Chart. CSL Signals from Rock vs. Clay, between Access Tubes 1 and 2 (Top), and Tubes 1 and 3 (Bottom)

4.5 CSL Wave Interaction with Rebar

Figures 4.10 – 4.15 compare CSL signals from a drilled shaft with no rebar with signals from a typical shaft with rebar. The purpose is in part to test the claim that rebar scatters and disrupts the signal, requiring access tubes be located inside the rebar cage.

Figure 4.10 shows the compression wave propagating from the top access tube after $20\ \mu\text{s}$. The concrete has lower density and stiffness than the rebar, resulting in the reverse-polarity difference shown in the difference plot. The actual reflection is the same polarity, but is shown reversed because of the order of the difference.

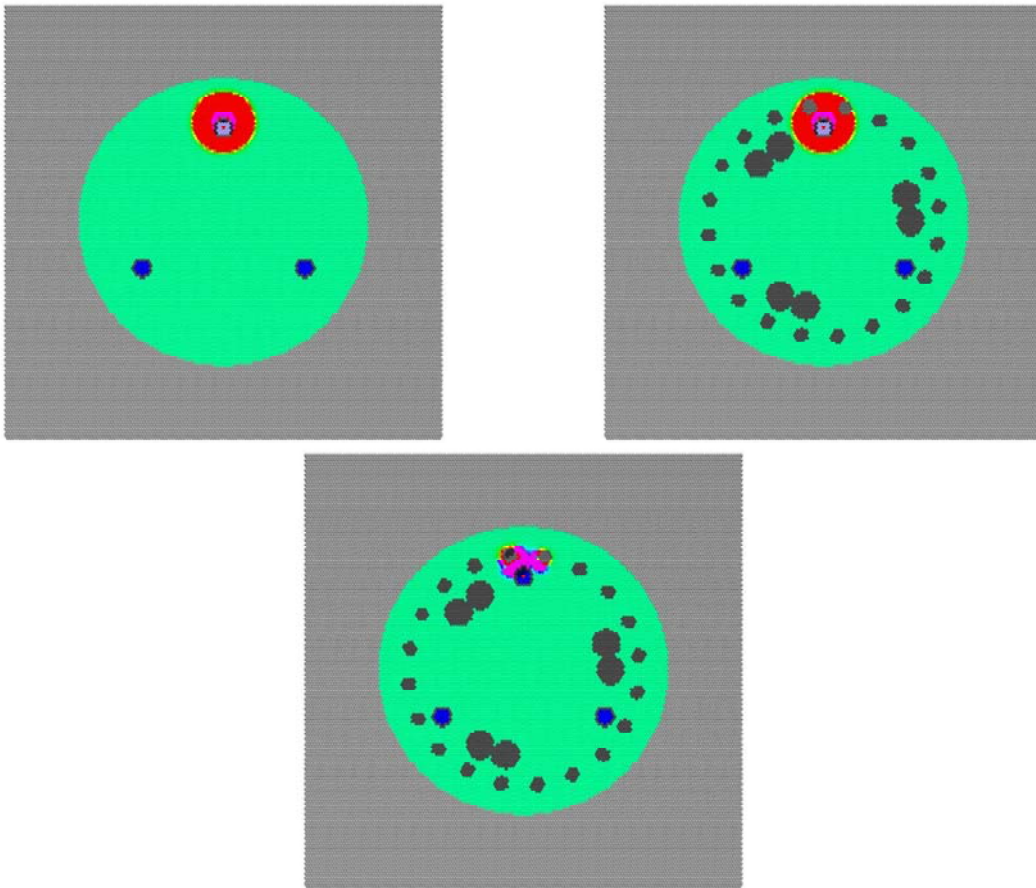


Figure 4.10. Plot. No Rebar (Top Left) vs. Rebar (Top Right) at $20\ \mu\text{s}$, with Difference (Bottom)

Figure 4.11 shows the compression wave at $60 \mu\text{s}$, as the wave first interacts with the surrounding ground. The rebar slightly deforms the wavefront, but the scattering does not destroy the compression wave entirely. The difference plot highlights the effects of the rebar.

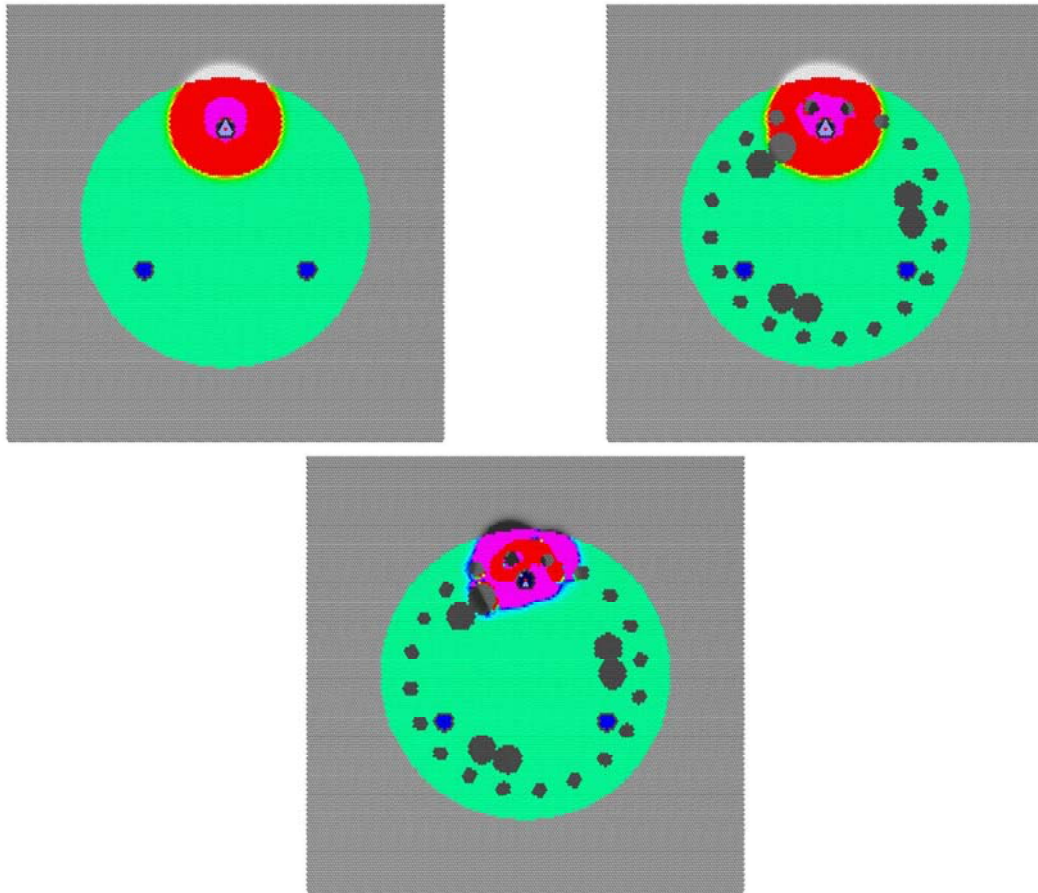


Figure 4.11. Plot. No Rebar (Top Left) vs. Rebar (Top Right) at $20 \mu\text{s}$, with Difference (Bottom)

Figure 4.12 shows the compression wave at $120 \mu\text{s}$, as the first tension wave interacts with the surrounding ground. The top plots show that the signal propagating into the rock is not noticeably affected after passing through the rebar.

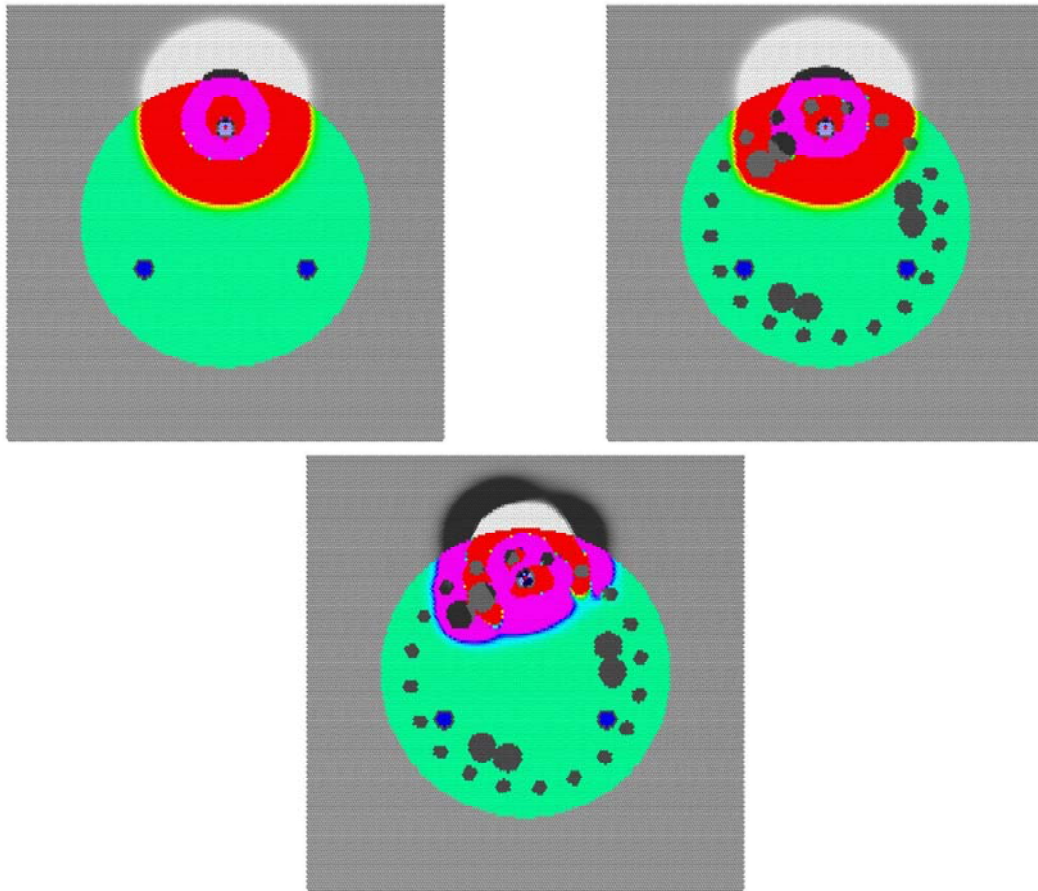


Figure 4.12. Plot. No Rebar (Top Left) vs. Rebar (Top Right) at $120 \mu\text{s}$, with Difference (Bottom)

Figure 4.13 shows the compression wave at 300 μ s, as the first compression wave reaches the access tubes. The arrival is practically identical for both access tubes. The difference plot shows the rebar does have a slight effect on the amplitude of the arrival, and will affect the rest of the waveform.

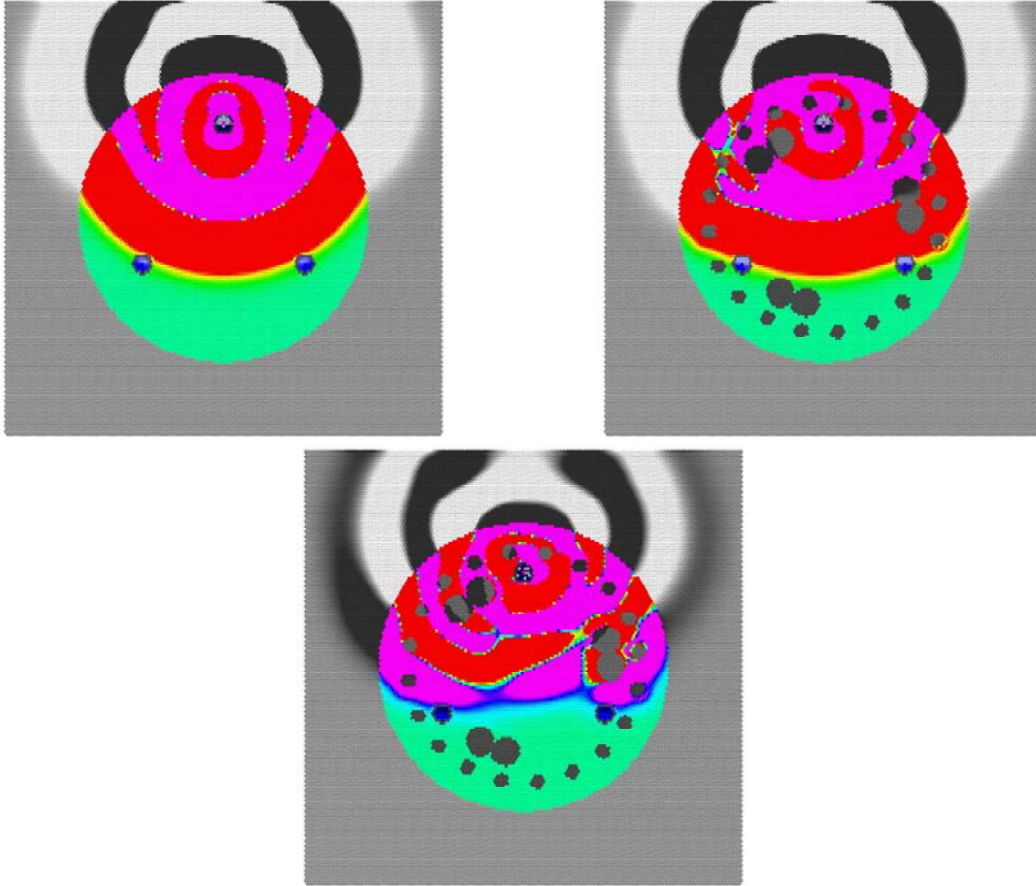


Figure 4.13. Plot. No Rebar (Top Left) vs. Rebar (Top Right) at 300 μ s, with Difference (Bottom)

Figure 4.14 shows the compression wave at 500 μ s, as the first tension wave reaches the access tubes. The first tension wave arrivals are essentially the same. The rebar does distort the wavefront, but the scattering is not significant for CSL purposes.

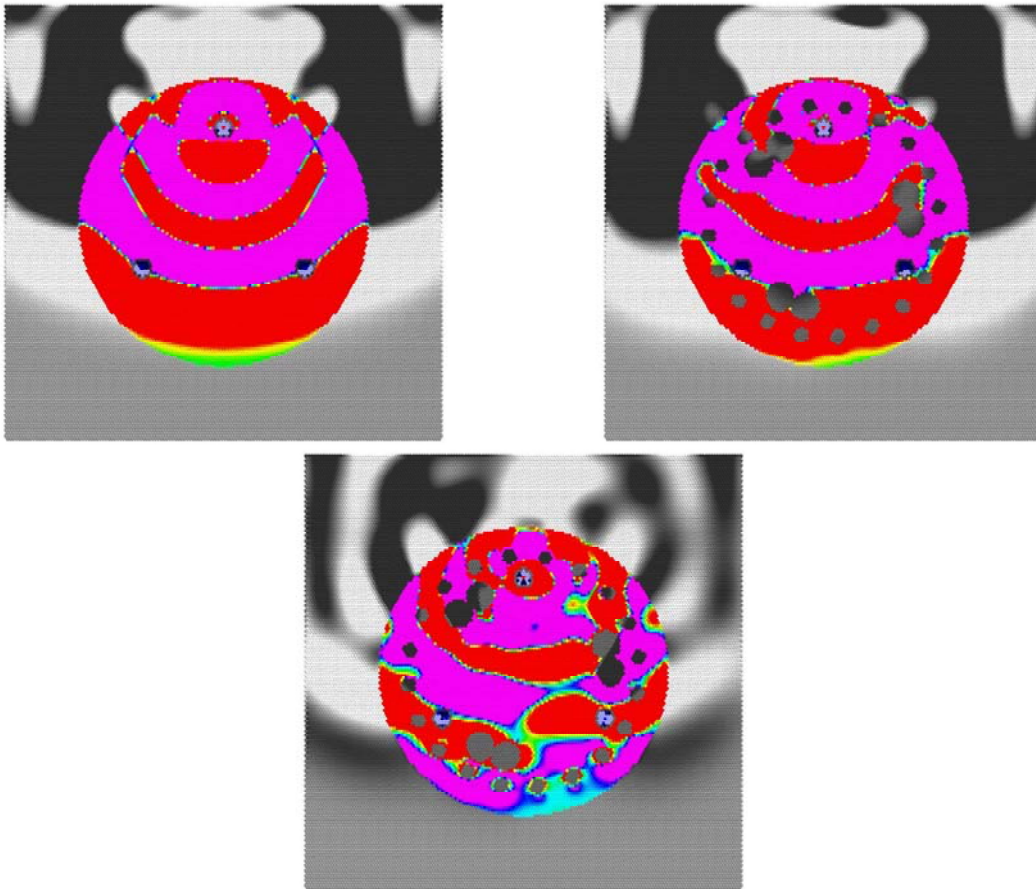


Figure 4.14. Plot. No Rebar (Top Left) vs. Rebar (Top Right) at 500 μ s, with Difference (Bottom)

Figure 4.15 compares the waveforms collected in the access tubes. Although the rebar theoretically does not influence the first arrival, the waveforms show that the rebar has a large enough effect on the subsequent waveform that it could affect the first arrival pick, depending on the person making manual picks, or on the picking algorithm if performed automatically. For CSL systems that simply plot the raw data, the effect of rebar could affect interpretation.

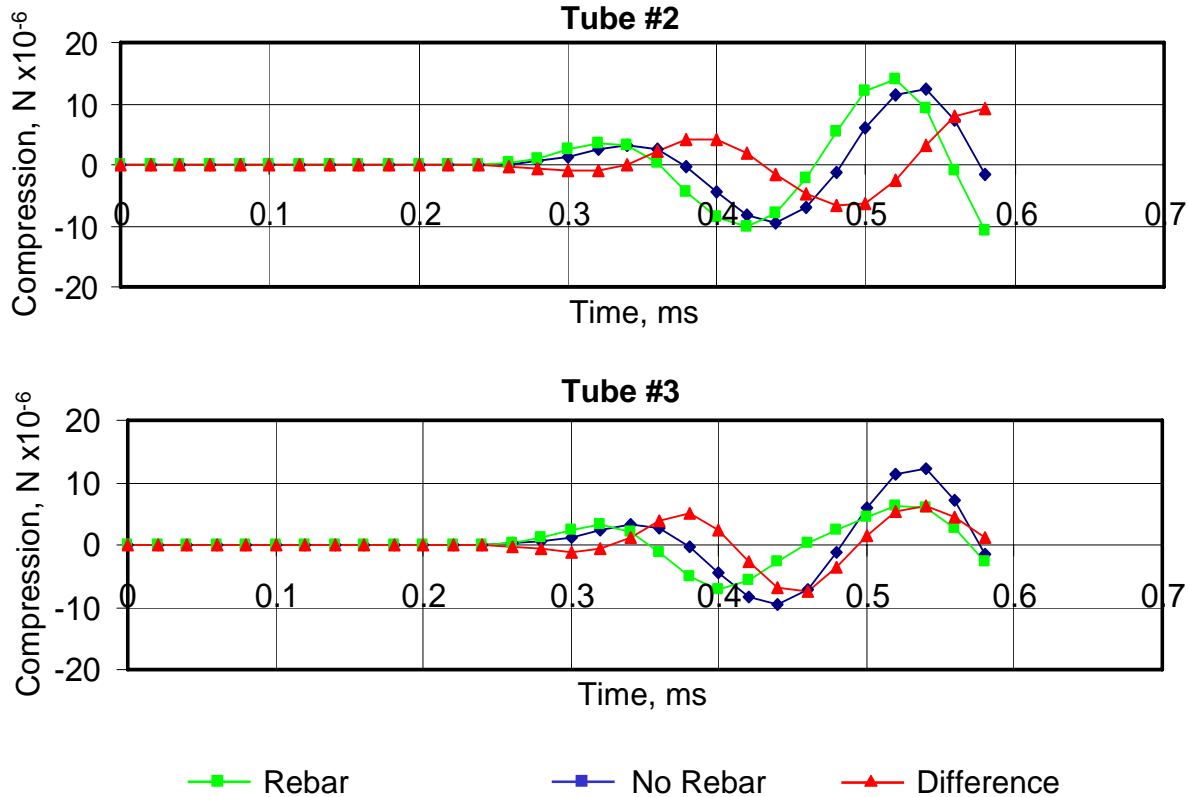


Figure 4.15. Chart. CSL Signals from No Rebar vs. Rebar, between Access Tubes 1 and 2 (Top), and Tubes 1 and 3 (Bottom)

4.6 Tube Effects

Access tubes can affect CSL velocity and energy in various ways. Numerical modeling can be used to quantify these effects. Different tube materials such as steel and PVC, with different thicknesses, can result in different waveforms. The effect of tube bending is significant. Tube deviation surveys are critical for eliminating these errors.

Tubes form a discontinuity in the concrete shaft. When filled with water or air, the tubes create a region of lower velocity that, unlike solid concrete, does not propagate shear waves. However, the previous numerical model study of the effects of rebar suggests that the tubes have minimal influence on the wave, and will not result in pronounced wave distortion, diffusion, reflection, or scatter.

Errors in the source and receiver location increase the probability of false defect classification, especially with tomographic reconstructions. Concrete is injected through the center of the drilled shaft during placement, and the pressure and flow of the concrete mix tends to displace tubes outward from the center. Eddy currents within the mix, together with vibrations during placement, can displace tubes unpredictably. Tubes may be bent prior to placing the mix due to the weight of the rebar support cage itself. This often results in unpredictable tube bending in the bottom of the shaft. Tubes also can bend near the surface, resulting in inaccurate measurements of tube separations deeper in the shaft.

When tubes bend away from the center, the tubes are farther apart than assumed. This increase in distance results in an increase in travel time and a corresponding decrease in observed velocity. Methods used to correct for these errors can be problematic as actual low-velocity regions may be eliminated unintentionally.

One technique to adjust for unexpected low-velocity readings is to adjust the tube separation measurements to produce a more acceptable result. Arrival picks may also be individually adjusted, or massaged, to remove unwanted artifacts. Other techniques, such as Tomographic Velocity Equalization¹, may be incorporated to correct for “cycle skipping” pick errors, or to account for tube bending.

Adjustment techniques such as these, no matter how sophisticated, cannot guarantee accurate results in every case. Tube bending can be accurately determined in some cases assuming the concrete is consistent. However, there are cases when tube bending and inconsistent concrete are indistinguishable. For example, suppose one competent drilled shaft has a pressure surge at a certain depth, bending all the tubes away from the center. Suppose another defective shaft has a bad slurry mix resulting in a lower velocity defect at a certain depth. Both sets of arrival time picks for these shafts could be identical. Both sets of density data and temperature measurements could be identical, because the tubes in the former shaft would be bent outward. Both shafts would be either rejected or accepted by these adjustment techniques. This could result in additional cost to determine that the competent shaft had bent tubes, or could result in an undetected defect.

The solution is not to modify arrival picks, guess at tube bending, or construct more sophisticated statistical analysis techniques. The solution is to incorporate more data, such as tube deviation measurements, into CSL surveys.

4.6.1 Tube Material: PVC versus Steel Tubes

Access tubes are generally made of steel or PVC. PVC is used primarily for superior signal quality.

¹ Defects in Drilled Shaft Foundations, (2000) FHWA CFLHD publication, February, pp 17-19.

Figures 4.16 – 4.21 compare CSL signals from a drilled shaft with PVC access tubes to signals from a shaft with steel tubes. This comparison requires a 3-D model to properly analyze the effects.

Figure 4.16 shows the compression wave propagating from the source access tube on the upper right after $20 \mu\text{s}$. The PVC model, with light blue access tubes, is on the left. The model with steel access tubes is on the right.

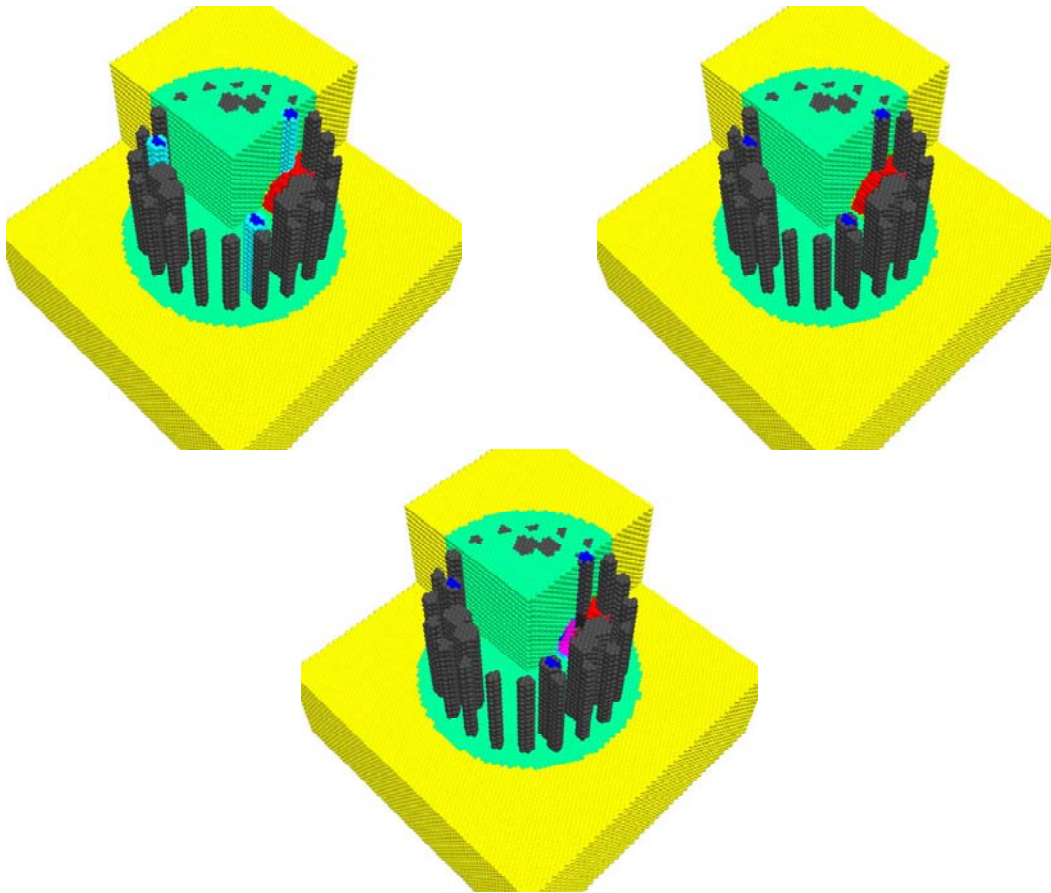


Figure 4.16. Plot. PVC (Top Left) vs. Steel (Top Right) Access Tubes at $20 \mu\text{s}$, with Difference (Bottom)

Figure 4.17 shows the compression wave at $60 \mu\text{s}$, as the wave first interacts with the surrounding ground. Both wavefronts appear similar, and differ only in amplitude.

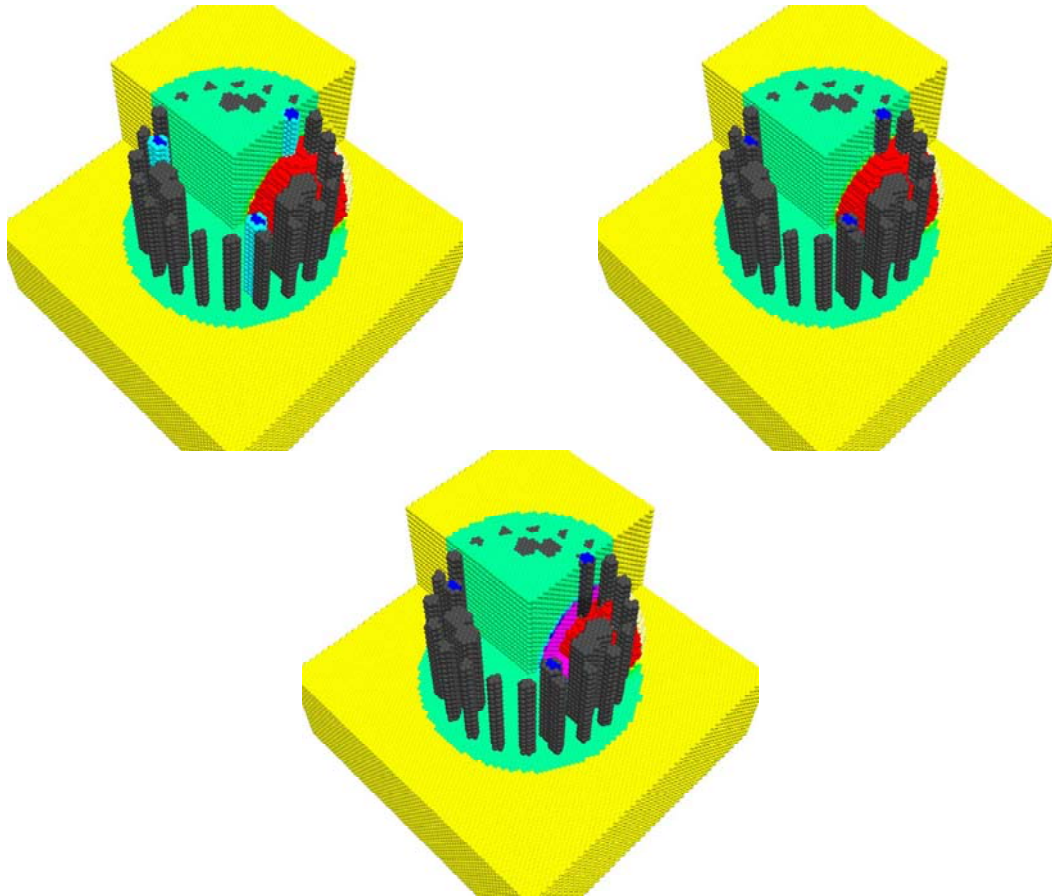


Figure 4.17. Plot. PVC (Top Left) vs. Steel (Top Right) Access Tubes at $20 \mu\text{s}$, with Difference (Bottom)

Figure 4.18 shows the compression wave at $120 \mu\text{s}$, as the compression wave approaches the receiver access tubes. The wavefronts are virtually identical in shape.

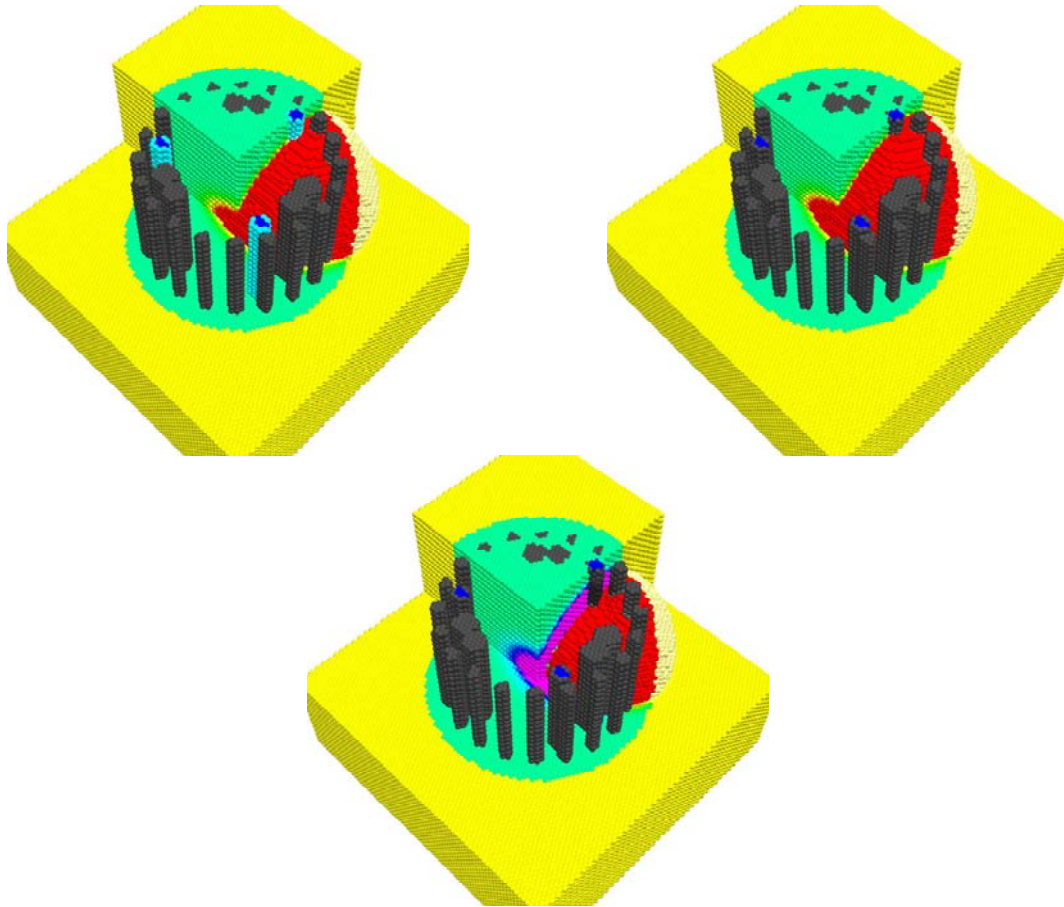


Figure 4.18. Plot. PVC (Top Left) vs. Steel (Top Right) Access Tubes at $120 \mu\text{s}$, with Difference (Bottom)

Figure 4.19 shows the compression wave at 300 μs , as the first compression wave reaches the receiver access tubes. The arrival is practically identical for both models.

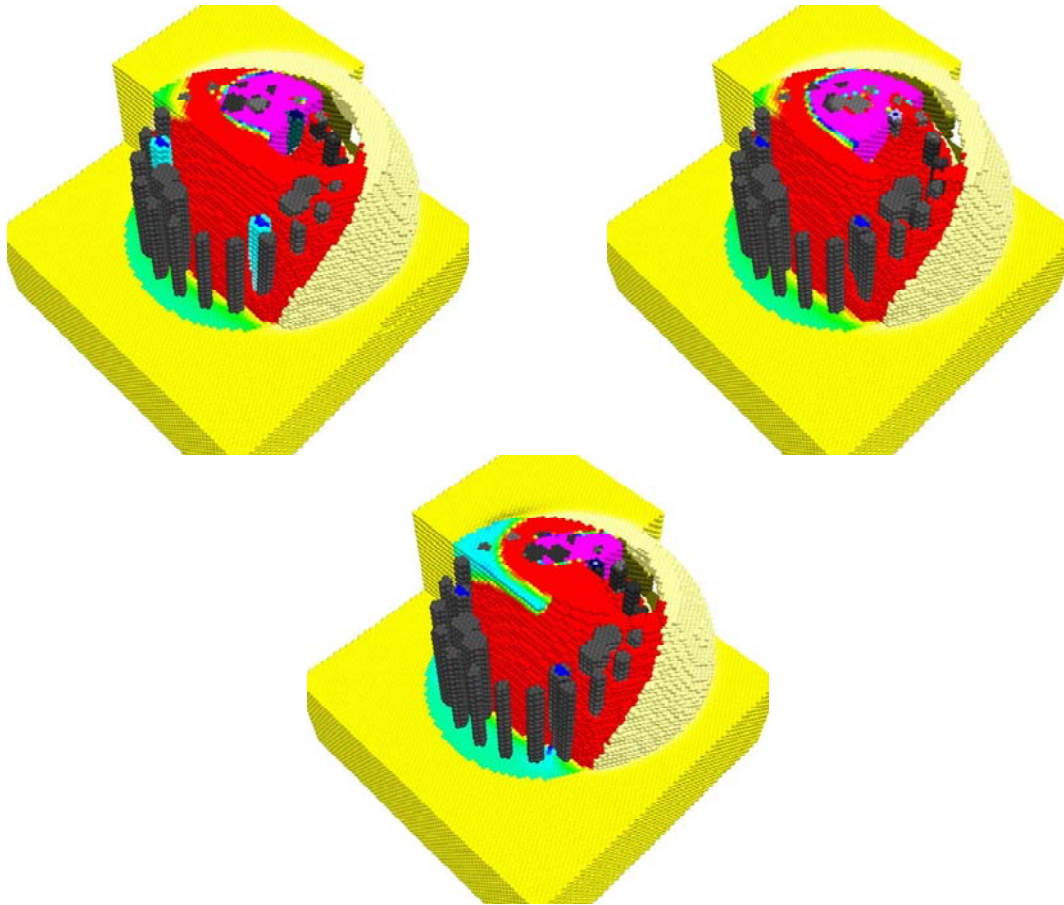


Figure 4.19. Plot. PVC (Top Left) vs. Steel (Top Right) Access Tubes at 300 μs , with Difference (Bottom)

Figure 4.20 shows the compression wave at 500 μs , as the first tension wave reaches the access tubes. The amplitude of the signal from the steel tubes is significantly less, but the wavefront shape remains similar.

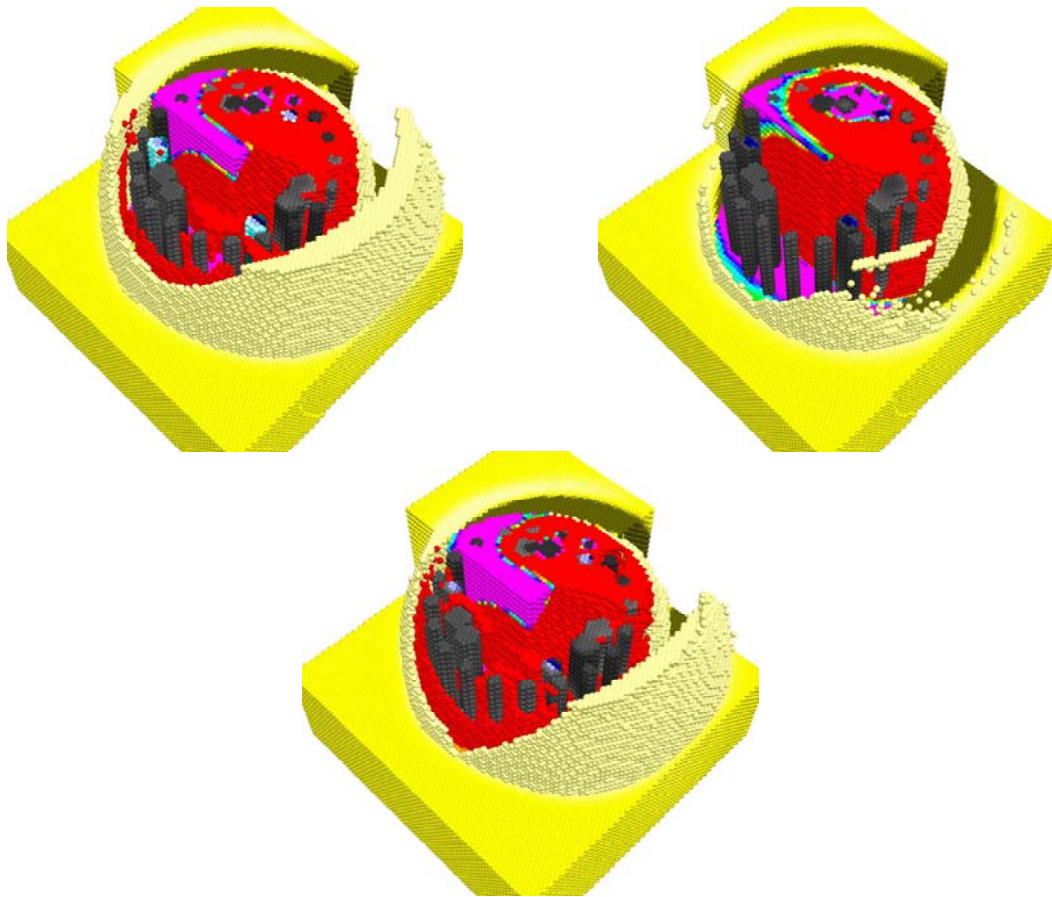


Figure 4.20. Plot. PVC (Top Left) vs. Steel (Top Right) Access Tubes at 500 μs , with Difference (Bottom)

Figure 4.21 compares the waveforms collected in the access tubes. The signal amplitude using PVC tubes is at least five times higher than steel. A larger portion of the compression wave energy is absorbed by the steel and transmitted up the tube rather than into the concrete, resulting in lower amplitude signals measured at the receiver. The first arrivals are the same, but the peak of the first compression wave is significantly different. The peak from the steel access tube arrives approximately 50 μ s before the peak from the PVC. This phenomenon will have significant effects on arrival picks based on the first compression peak.

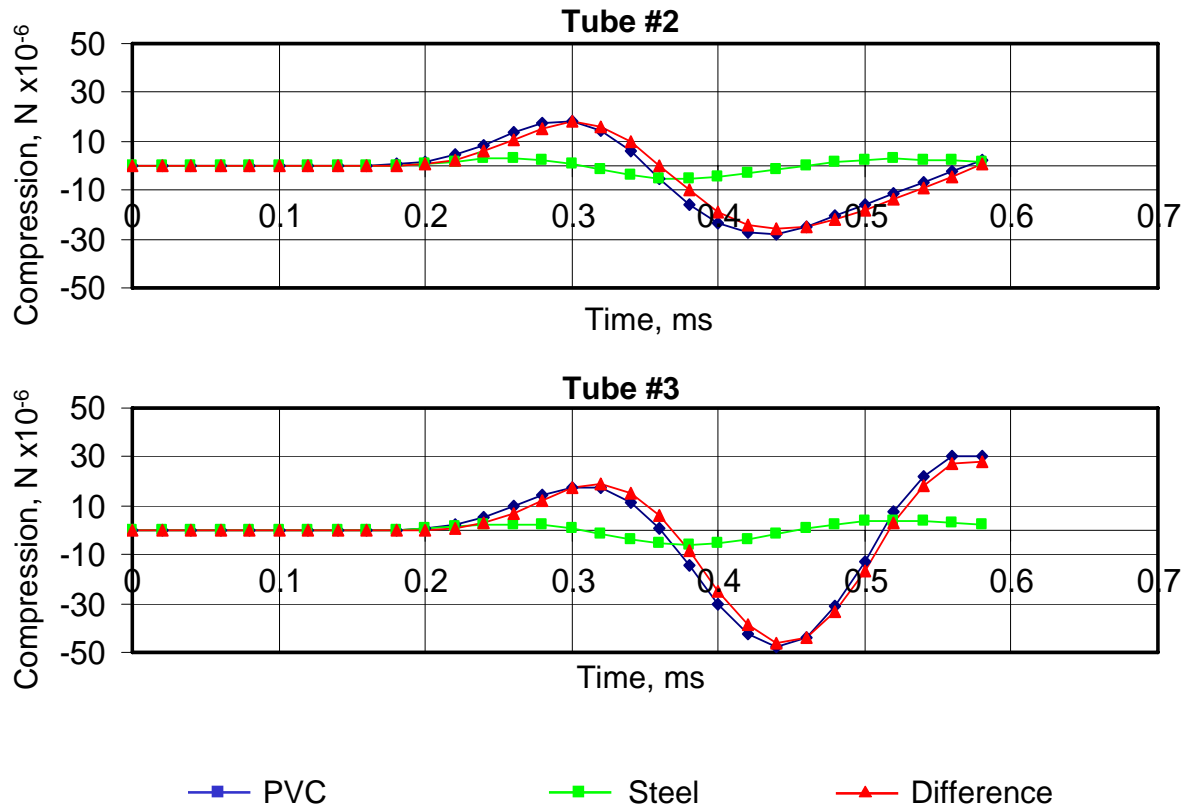


Figure 4.21. Chart. CSL Signals from PVC vs. Steel Access Tubes, between Tubes 1 and 2 (Top), and Tubes 1 and 3 (Bottom)

Although PVC transmits a higher amplitude signal, PVC is easily broken during concrete placement, preventing CSL surveys from being conducted. PVC also has a thermal expansion five times higher than steel, as shown in Table 4.3. For this reason, the use of PVC often results in tube debonding in a short period of time as the shaft cools. PVC is more brittle than steel, and occasionally is broken during placement. PVC also can be crushed by the shrinking concrete during the curing process. Some agencies still use PVC, but because of the disadvantages of using PVC, and because steel tubes are becoming more widely used, the remainder of the models in this study will use steel access tubes.

Table 4.3 Thermal Expansion of PVC and Steel (inches/100 ft)²

Temperature Change °F	PVC	Steel
25	0.9	0.18
50	1.8	0.36
75	2.7	0.54
100	3.6	0.72
150	5.4	1.08

4.6.2 Tube Debonding

Debonding conditions between the tubes and the concrete occasionally occur in a shaft for various reasons. One common cause is initial tube expansion during the curing process due to heat from concrete hydration, followed by contraction of the tube as the concrete cools. The vertical expansion is much greater than the radial expansion, causing tubes to slide vertically, breaking contact bonds at the tube/concrete interface. Since tubes usually are anchored in the bottom of the shaft due to initial concrete placement, the largest vertical displacement will occur in the upper portion of the shaft. Tubes disturbed after concrete placement can also result in tube debonding in the upper portion of the shaft. However, the most common cause of tube debonding is due to thermal expansion, especially when PVC access tubes are used.

Tube debonding in upper regions can also be caused by mechanically induced stress, such as bending or impacting the access tubes. Tube debonding can also occur even when tubes are not disturbed during the curing process. If the top of the shaft is not well insulated or the tubes are not filled with water immediately after concrete placement, large temperature gradients can form within the concrete. The gradient is especially severe in the region of the tubes because the tubes readily transmit heat to the surface. Large temperature gradients may also result in severe micro cracking and reduce the strength of concrete in the foundation.

Tubes should be filled with clean drinking water before or shortly after concrete placement. Filling tubes with water inhibits the debonding of the concrete from the tube. Tube debonding occurs when heat is dissipated too quickly, creating a large temperature gradient surrounding the tube. A large temperature gradient results in cracking, not only from added stresses from tube shrinkage, but also from internal cooling induced stresses in the concrete. Water has a higher specific heat than air and provides the necessary insulation to reduce the temperature gradient to acceptable levels. A rule of thumb in construction practice is to add water to the tubes within one hour after concrete placement. However, the first hydration phase of the curing process completes within the first 15 minutes, so water should be added before or as soon as possible after concrete placement.

Stress on the tubes before curing can also cause tube debonding. Excess torque or impacts during removal or replacement of tube caps or plugs can result in stresses that break the bond between the tubes and the concrete, even deep within the drilled shaft. So, care must be taken to avoid this problem.

² http://www.engineeringtoolbox.com/thermal-expansion-pvc-14_782.html

Tube debonding can significantly attenuate signals at both the source and receiver, resulting in reduced velocity measurements or lost data. Examining only the first arrival and signal amplitude is not adequate for distinguishing tube debonding from actual defects. Full waveform inversion techniques should be employed to accurately reconstruct the occurrence and extent of tube debonding.

Although initial tube debonding may appear harmless, the micro-cracks provide an inlet for future contaminants to enter and corrode the internal structure of the concrete and rebar support. Tube debonding can form and extend long after concrete curing, due to shaft deformation from loading stresses, ground settlement, freeze-thaw cycles, exposure to contaminants, and thermal expansion and contraction of the shaft and the surrounding environment.

The concrete in the shaft should normally be allowed to cure at least 1-2 days prior to testing. If PVC tubes are used, testing should be done within 10 days after the placement of concrete due to possible tube-concrete debonding. If steel tubes are used, testing can be done within 45 days after concrete placement as the steel tubes bond better than PVC tubes over a longer time.

Although CSL does require installation of tubes that could compromise the durability and performance of concrete in the long term, the same debonding issues apply to rebar within the concrete. In any event, care should be taken to avoid detrimental long-term effects.

Extreme tube debonding should be a serious concern. However, very slight tube debonding can be difficult to detect, but still can result in serious long-term effects.

Figures 4.22 – 4.27 compare CSL signals from a drilled shaft with tube debonding defects to signals from a shaft with no defect. This comparison requires a 3-D model to properly analyze the effects. A 0.5 m tube debonding defect is placed around the source access tube 1 and tube 2. The defect extends 0.25 m above and below the source and receiver.

Figure 4.22 shows the compression wave propagating from the source access tube on the upper right after 20 μ s. The debonding defect significantly blocks wave propagation at the source.

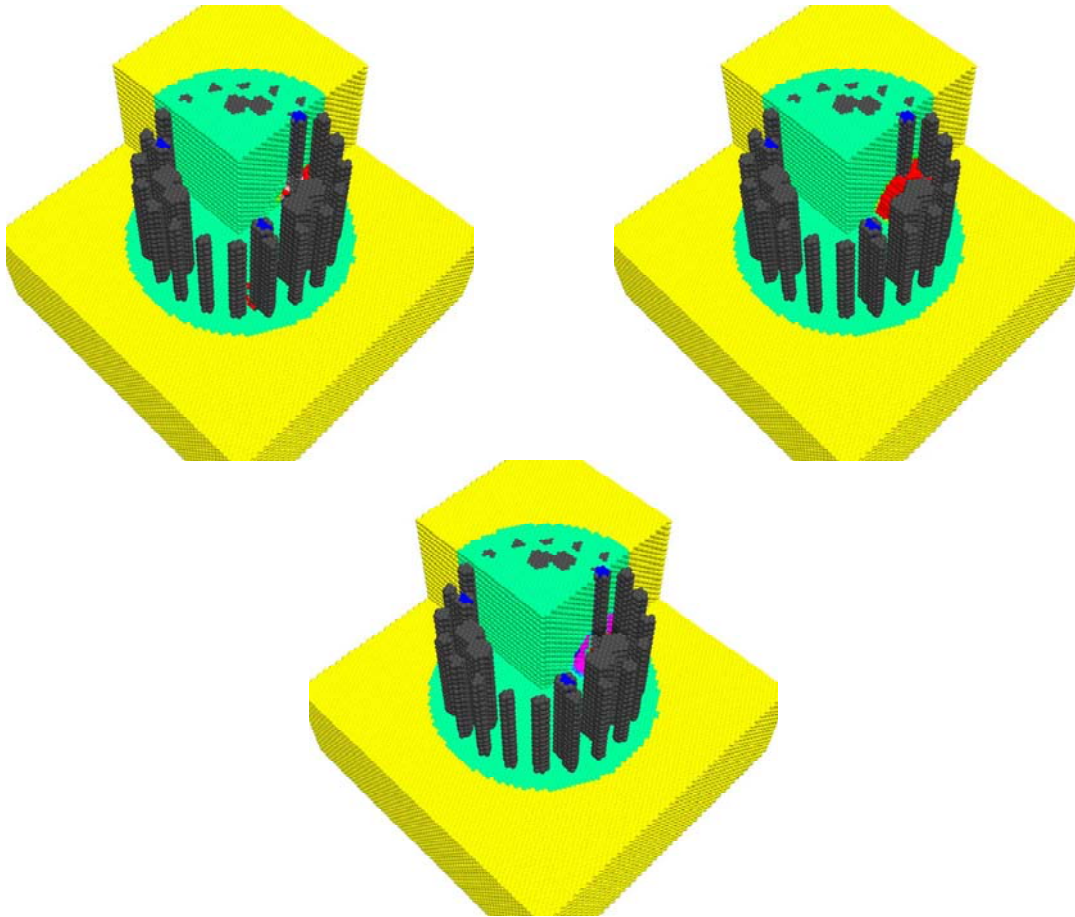


Figure 4.22. Plot. Tube Debonding (Top Left) vs. No Tube Debonding (Top Right) at 20 μ s, with Difference (Bottom)

Figure 4.23 shows the compression wave at $60 \mu\text{s}$, as the wave first encounters the surrounding ground. The signal has been significantly delayed and attenuated by tube debonding.

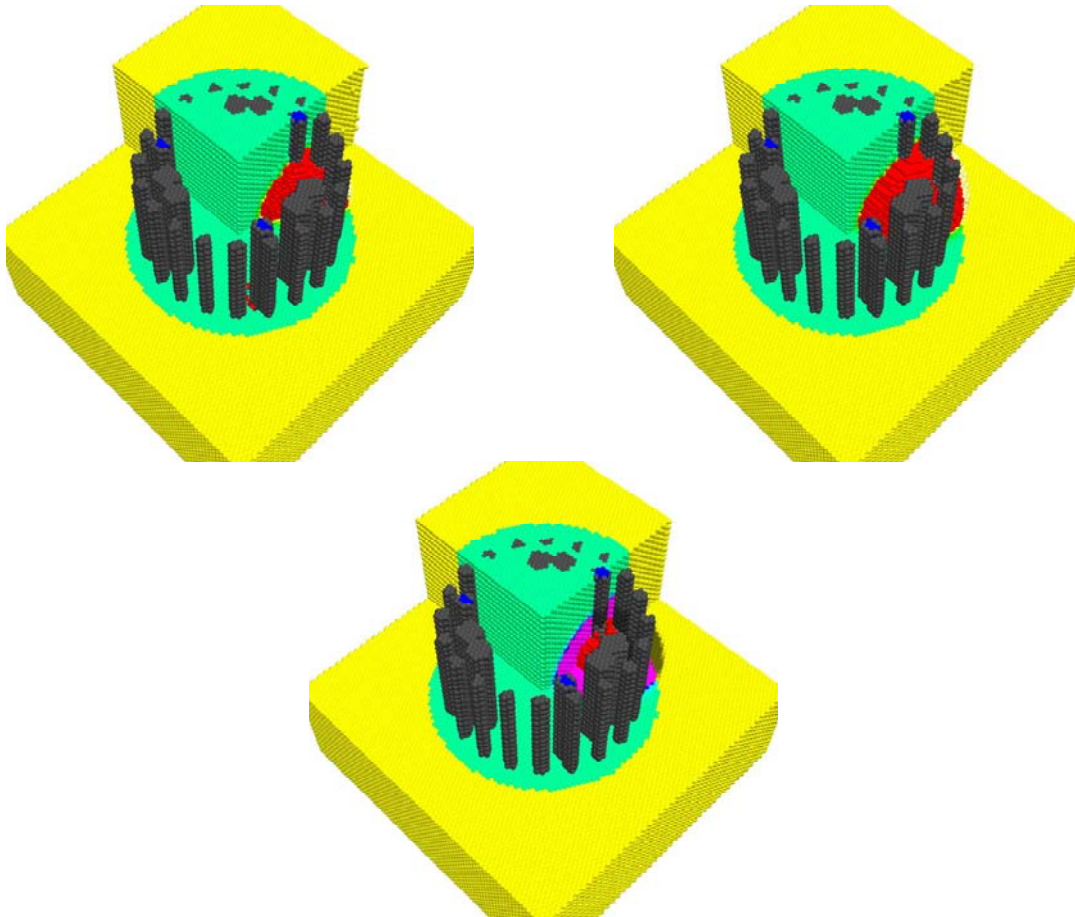


Figure 4.23. Plot. Debonding (Top Left) vs. No Tube Debonding (Top Right) at $20 \mu\text{s}$, with Difference (Bottom)

Figure 4.24 shows the compression wave at 120 μ s, as the compression wave approaches the receiver access tubes. The debonding defect had distorted the shape of wavefront, as much of the wave must travel along the tube and around the defect.

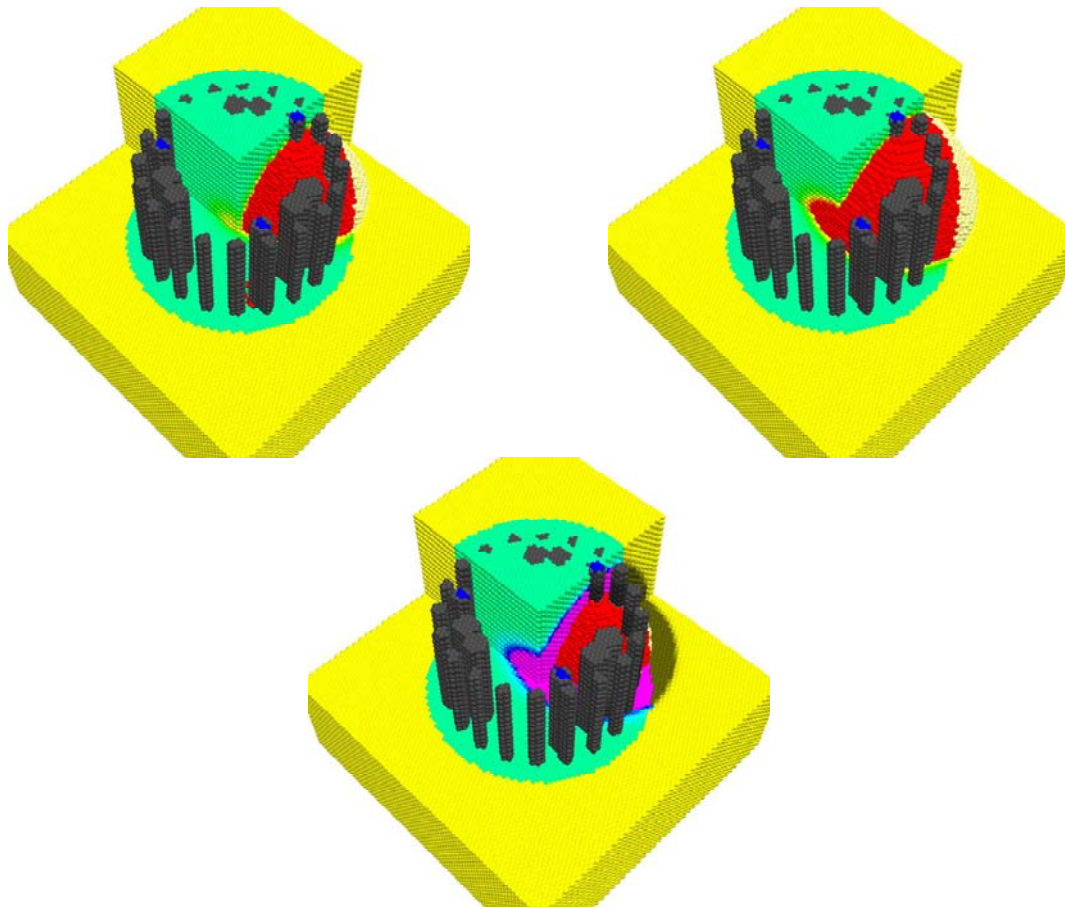


Figure 4.24. Plot. Debonding (Top Left) vs. No Tube Debonding (Top Right) at 120 μ s, with Difference (Bottom)

Figure 4.25 shows the compression wave at $300 \mu\text{s}$, as the first compression wave in the shaft with no tube debonding reaches the receiver access tubes. The first compression wave in the defective shaft is delayed, but has grown significantly higher in amplitude.

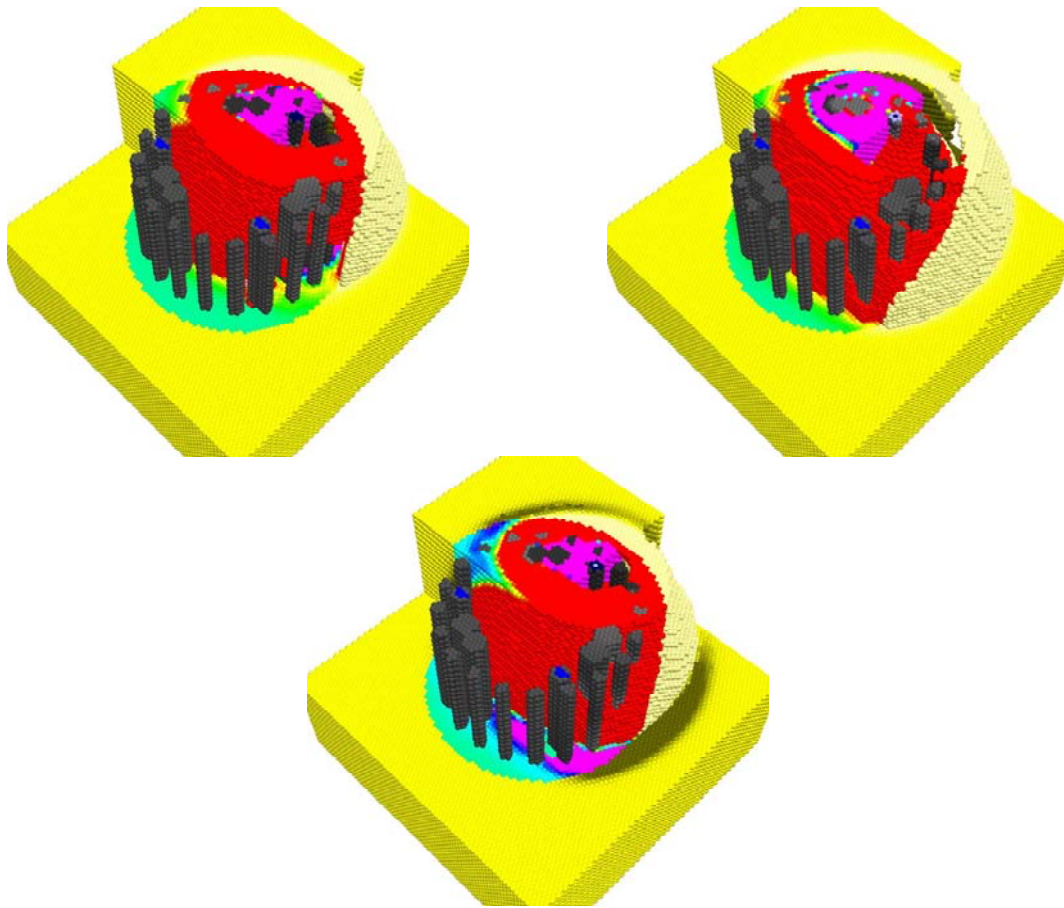


Figure 4.25. Plot. Debonding (Top Left) vs. No Tube Debonding (Top Right) at $300 \mu\text{s}$, with Difference (Bottom)

Figure 4.26 shows the compression wave at 500 μ s, as the first tension wave reaches the access tubes in the shaft with no debonding defect. The peak of the first compression wave now appears to have reached the access tubes in the defective shaft.

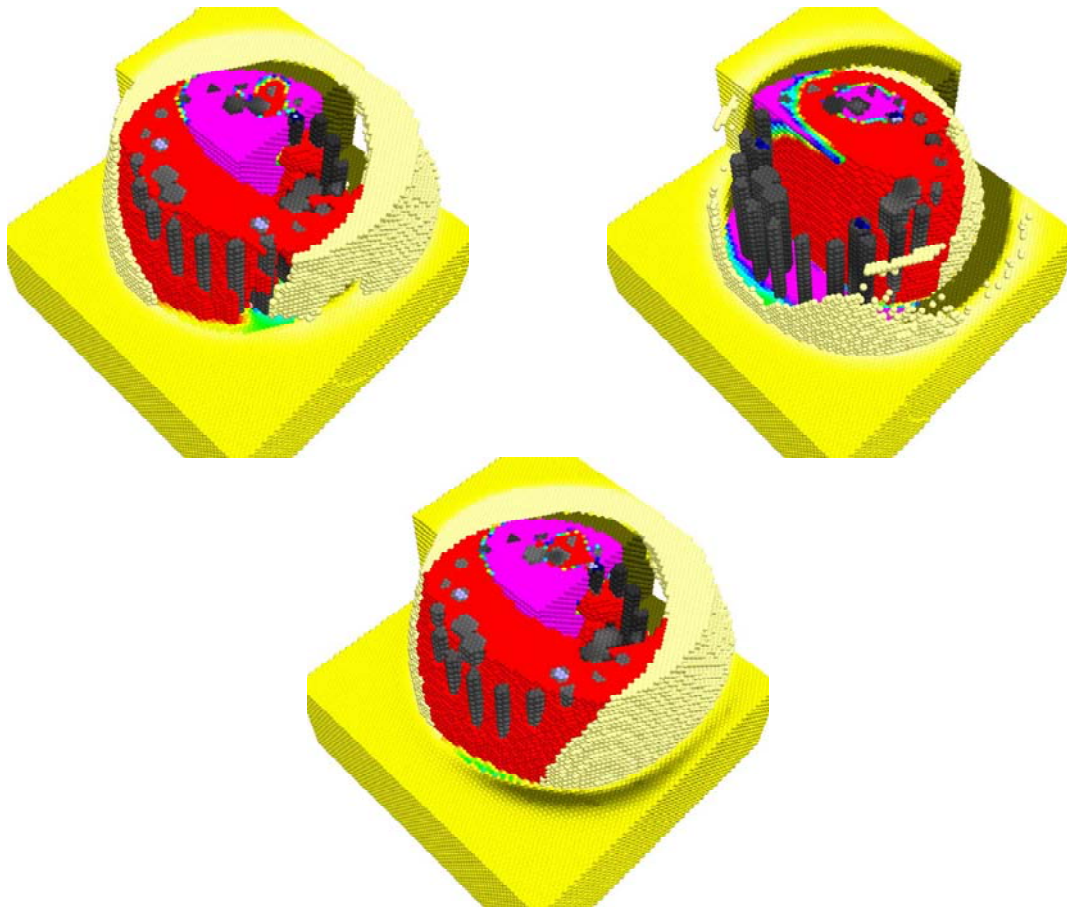


Figure 4.26. Plot. Debonding (Top Left) vs. No Tube Debonding (Top Right) at 500 μ s, with Difference (Bottom)

Figure 4.27 compares the waveforms collected in the access tubes. The top graph shows that the signal almost completely attenuates with tube debonding around both the source and receiver access tubes. The bottom graph shows a significant delay in the first compression peak from the source tube debonding. However, the amplitude of the signal in the tube with the debonding defect is significantly higher for some reason.

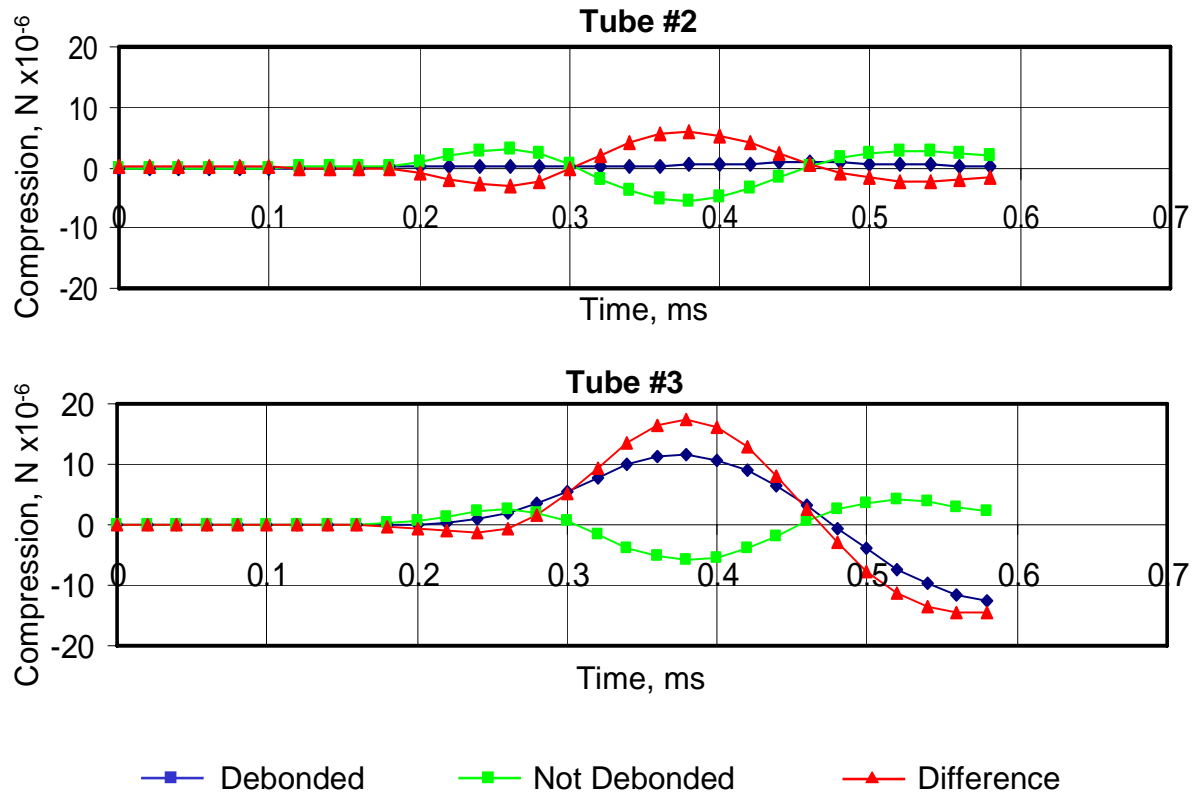


Figure 4.27. Chart. CSL Signals with Tube Debonding vs. No Tube Debonding, between Access Tubes 1 and 2 (Top), and Tubes 1 and 3 (Bottom)

4.6.3 Sensor Drift within the Access Tubes

Source and receiver position and orientation within the access tubes can have a significant effect on arrival time. The compression wave velocity of water is much lower than the velocity of concrete, so very small changes in the source or receiver position or rotation within the access tube can have a large effect on the arrival time. The numerical model estimates changes in velocity at levels up to 20% for only a 2 cm difference in source and receiver position.

Figures 4.28 – 4.33 compare CSL signals from a drilled shaft with the source and receivers displaced in the access tube 1 cm to the outside of the shaft, to a model with the source and receivers displaced 1 cm toward the center of the shaft. In this scenario, the signals travel a total difference of 4 cm through water.

Figure 4.28 shows the compression wave propagating from the top access tube after 20 μs . The model on the left, with the outside sensor drift, has an initial wavefront that is offset slightly higher than the model with inside sensor drift.

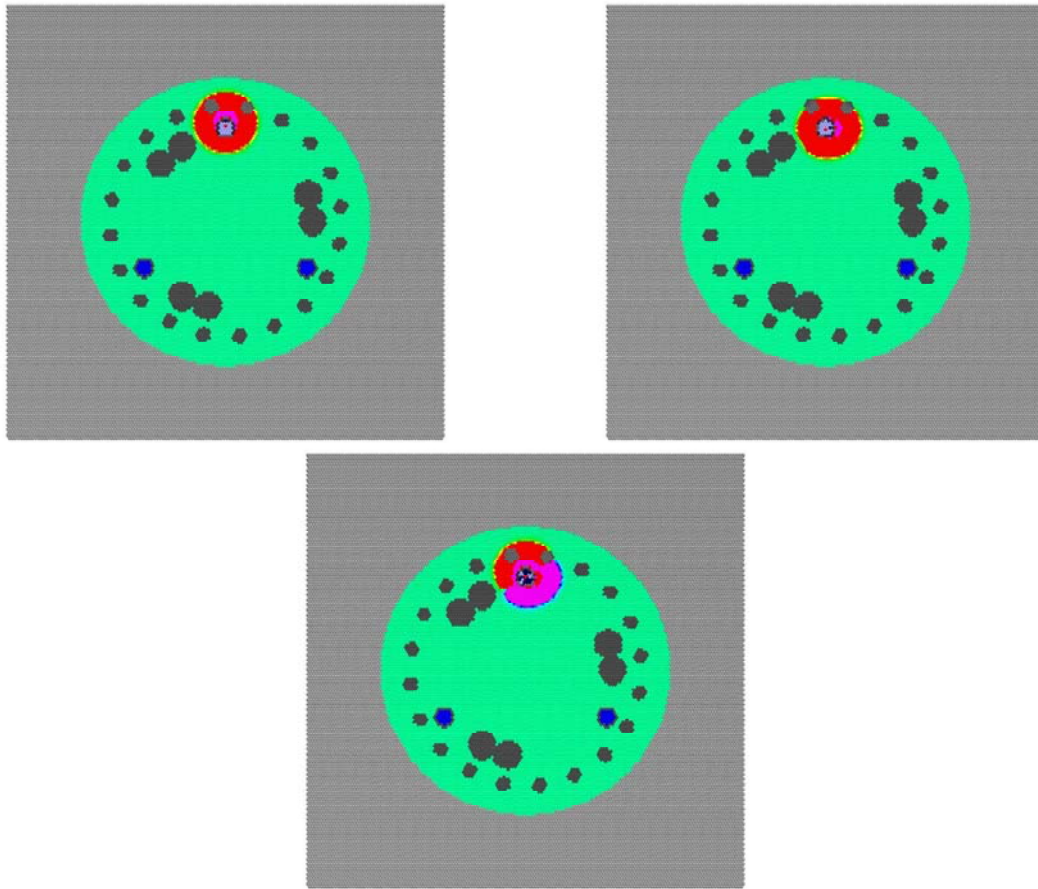


Figure 4.28. Plot. Outside Sensor Drift (Top Left) vs. Inside Sensor Drift (Top Right) at 20 μs , with Difference (Bottom)

The subsequent wavefront propagation is shown in Figures 4.29-4.32. The wavefront is slightly delayed in the model with outside sensor drift. The delay increases as the compression wave interacts with the water in the access tube.

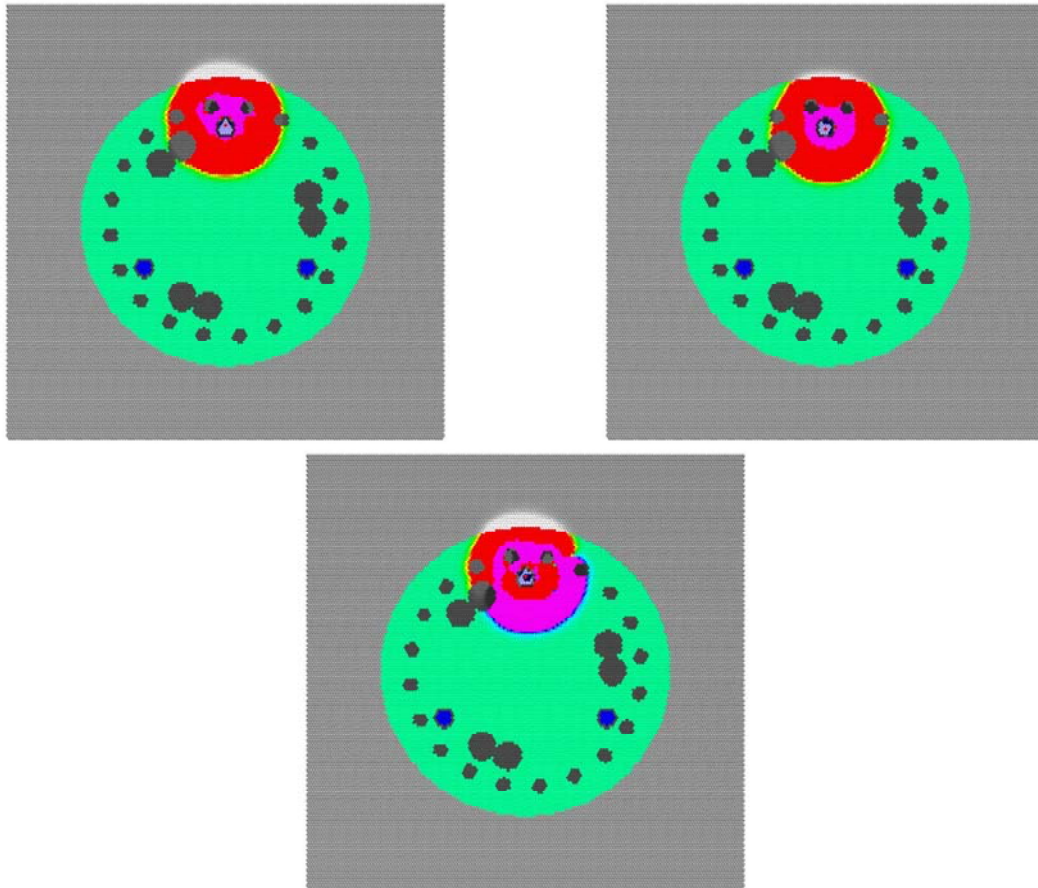


Figure 4.29. Plot. Outside Sensor Drift (Top Left) vs. Inside Sensor Drift (Top Right) at 20 μ s, with Difference (Bottom)

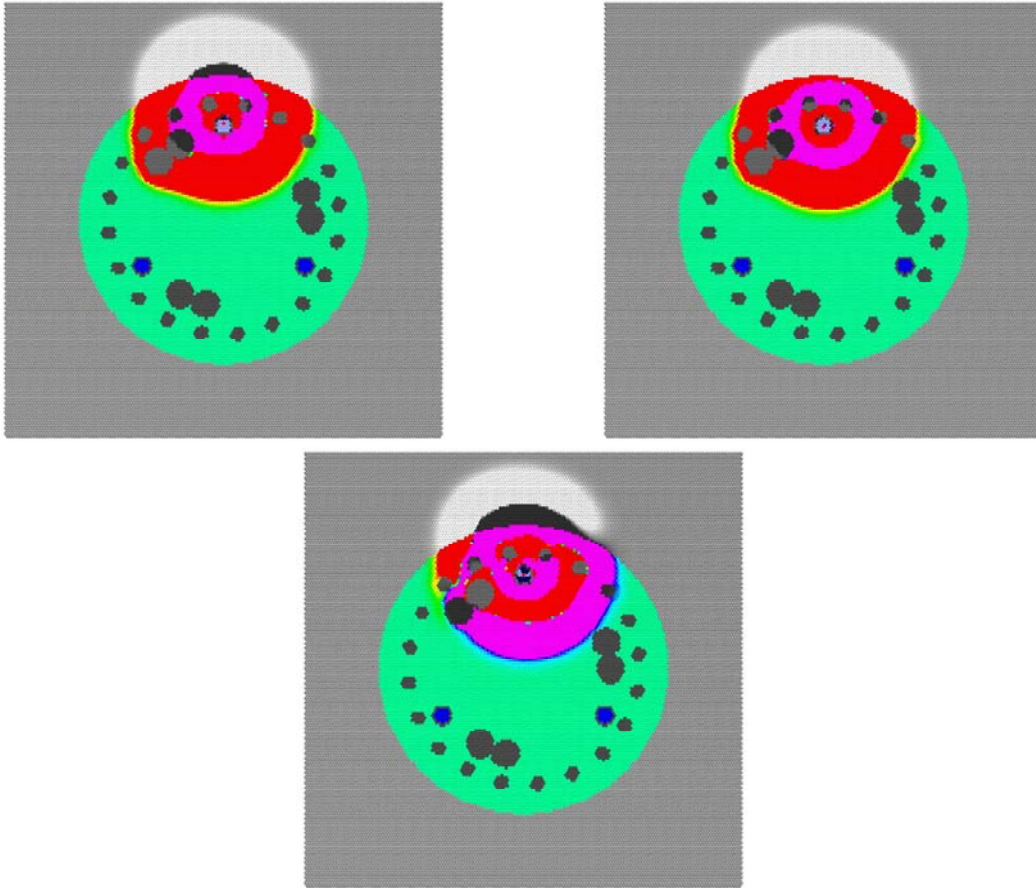


Figure 4.30. Plot. Outside Sensor Drift (Top Left) vs. Inside Sensor Drift (Top Right) at 120 μ s, with Difference (Bottom)

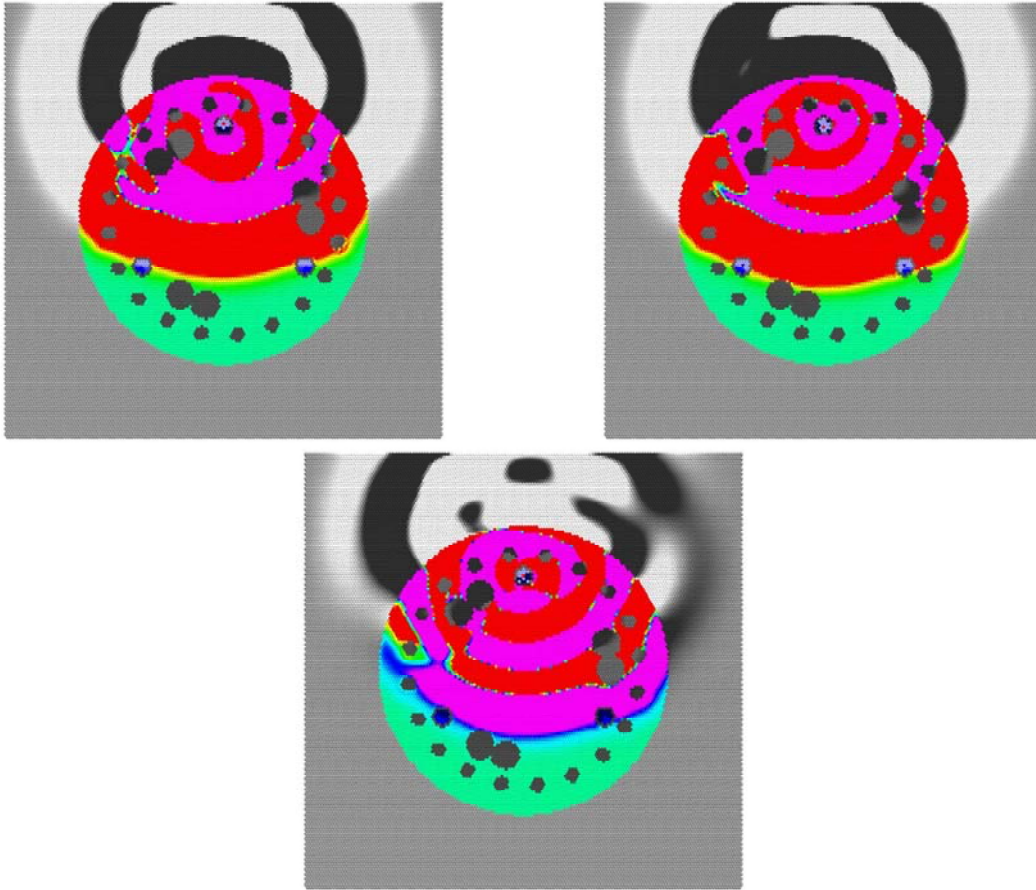


Figure 4.31. Plot. Outside Sensor Drift (Top Left) vs. Inside Sensor Drift (Top Right) at 300 μ s, with Difference (Bottom)

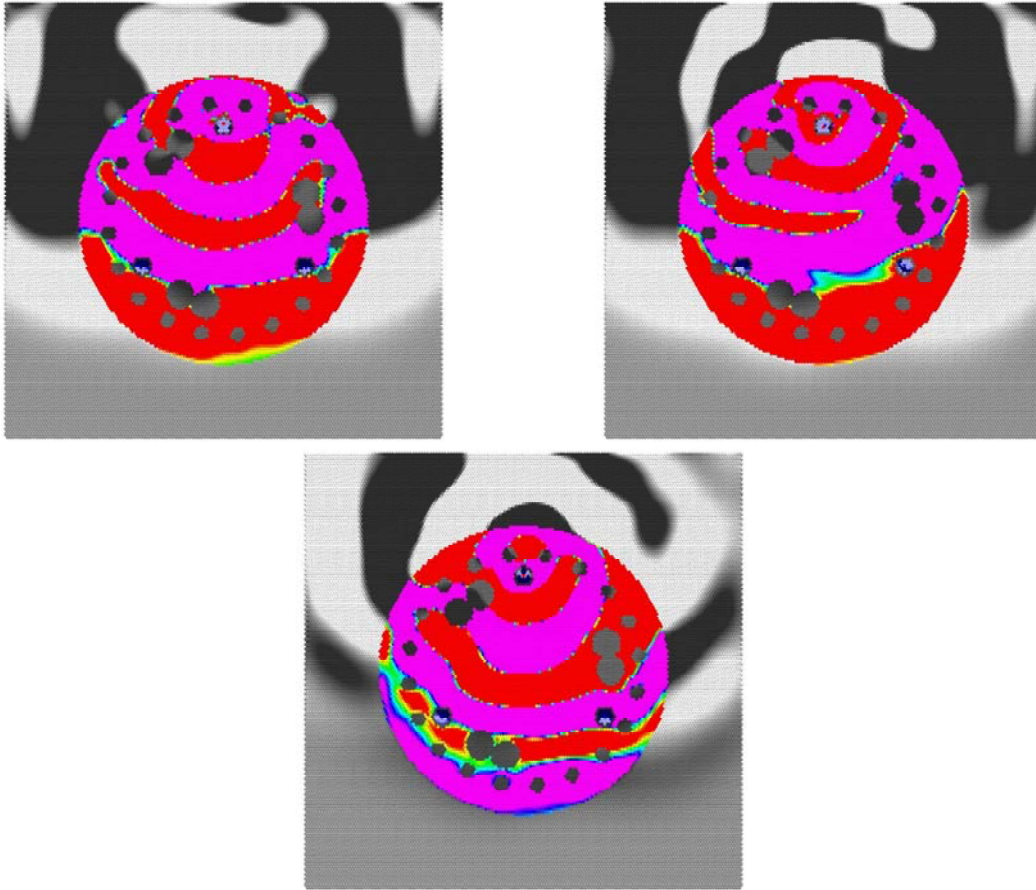


Figure 4.32. Plot. Outside Sensor Drift (Top Left) vs. Inside Sensor Drift (Top Right) at 500 μ s, with Difference (Bottom)

Figure 4.33 compares the waveforms collected in the access tubes. The top graph shows significant delay in the signal with outside sensor drift. The signal is also lower in amplitude and lower in frequency, due to the longer distance. This example shows the importance of carefully specifying tolerances in CSL data collection equipment if accurate measurements are desired.

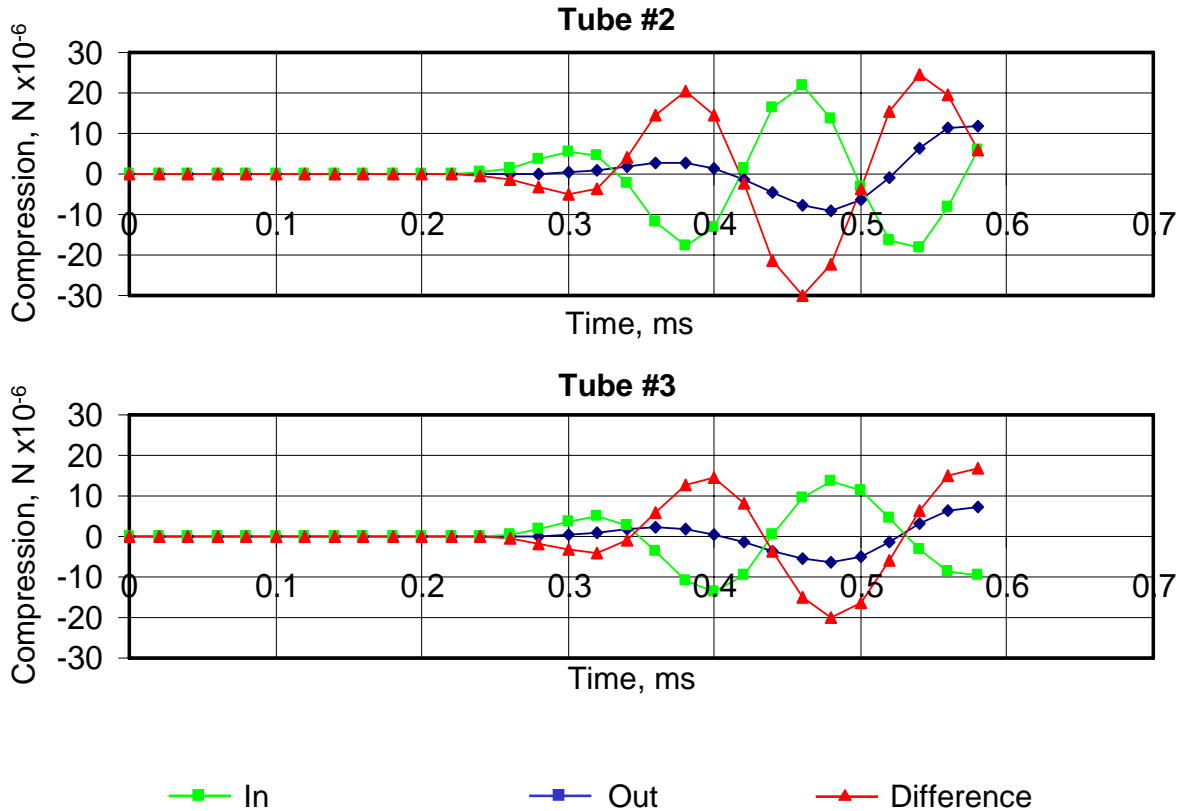


Figure 4.33. Chart. CSL Signals with Outside Sensor Drift vs. Inside Sensor Drift, between Access Tubes 1 and 2 (Top), and Tubes 1 and 3 (Bottom)

4.7 Concrete Cracking Effects

The inherently brittle nature of concrete makes cracking the most observable and characteristic defect of concrete structures. However, cracking can pass undetected using CSL first arrival and signal energy measurements in the field. Ultrasonic Pulse Velocity (UPV) lab tests are also not significantly affected by cracking, resulting in the characteristically poor ability of the test to predict concrete strength.

The effect of cracking on compression wave velocity is important to consider. When cracks are closed and under compression, and the compression wave is unable to open the crack, the velocity will not change. When the compression wave is unable to close an open crack, the wave will not propagate across the crack. If the wave can travel around the crack, the velocity will appear slower. When the compression waves is able to both open and close the crack, then the velocity will increase, and the amplitude of the first compression arrival will increase. This may seem counterintuitive, but logically follows because cracks under this condition do not contribute the same tensile force as intact material.

Figures 4.34 – 4.39 compare CSL signals from a drilled shaft with a cracking defect, shown in red, to a shaft with no defect. The cracking defect has the same compression wave velocity, modeled with 90% of the springs broken.

Figure 4.34 shows the compression wave propagating from the source access tube after 20 μ s.

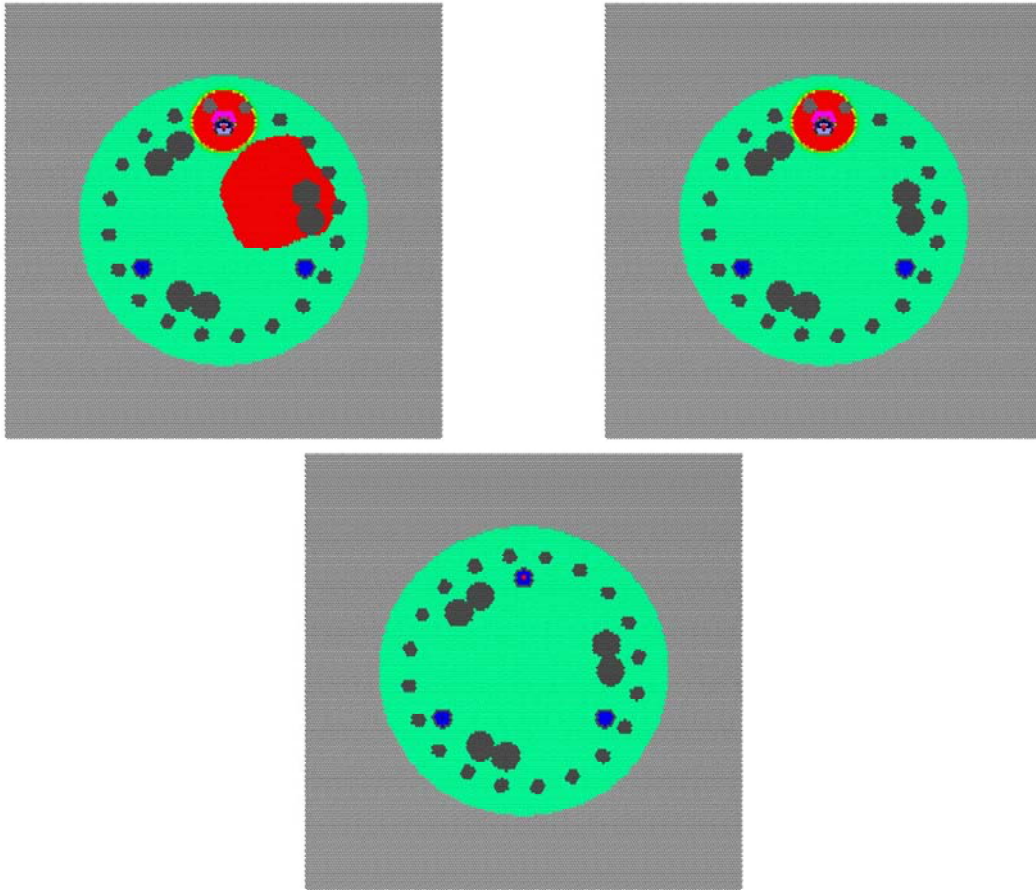


Figure 4.34. Plot. Cracking Defect (Top Left) vs. No Defect (Top Right) at 20 μ s, with Difference (Bottom)

The wavefront first encounters the cracking defect in Figure 4.35 at 60 μs . The difference plot shows the effect of the cracking on the compression wave.

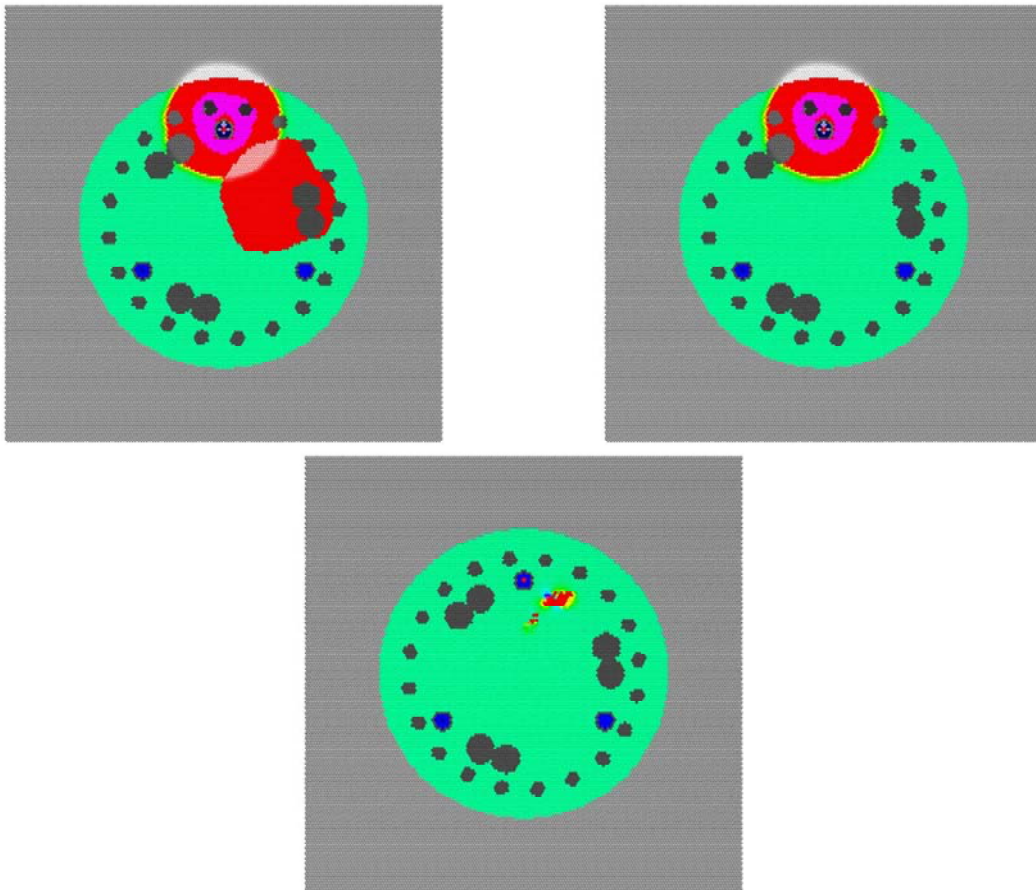


Figure 4.35. Plot. Cracking Defect (Top Left) vs. No Defect (Top Right) at 20 μs , with Difference (Bottom)

Figure 4.36 shows the compression wave at 120 μs , as the compression wave passes half way through the cracking defect. The amplitude of the compression wave is higher through the cracking defect, as shown in the difference model. This is the case because no tension forces “pull back” elements that are cracked, resulting in a higher degree of compression on the wave front.

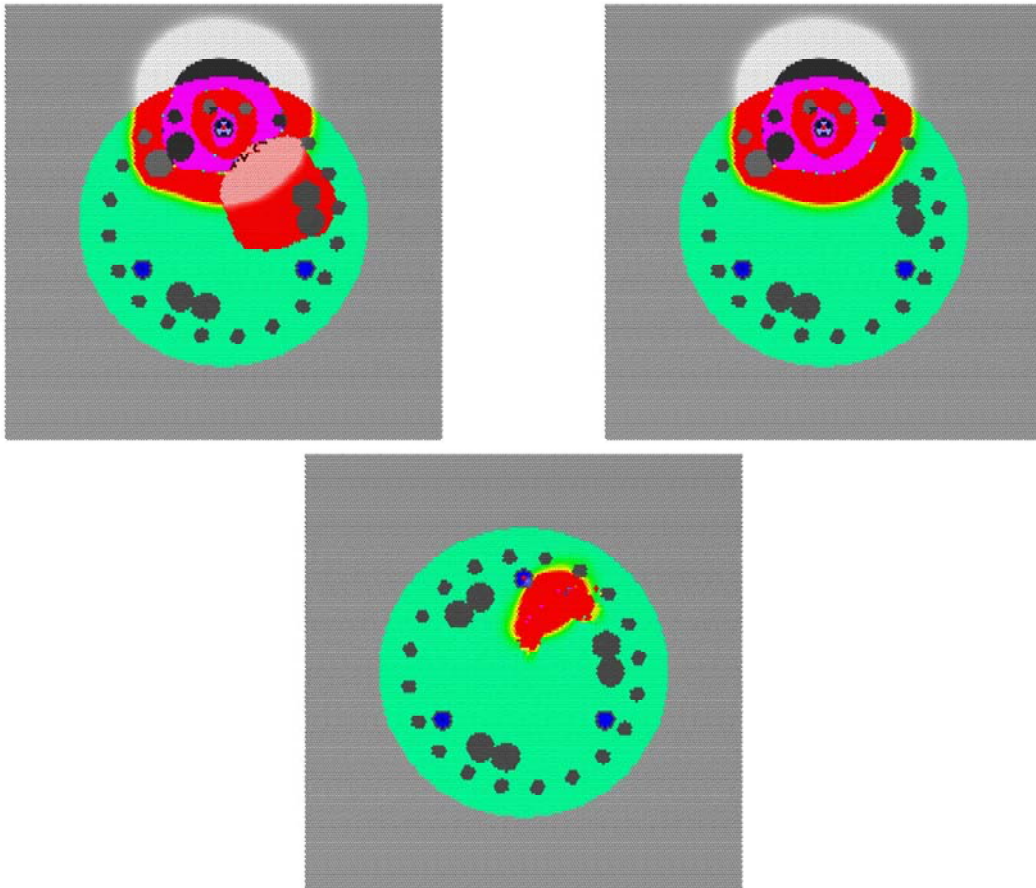


Figure 4.36. Plot. Cracking Defect (Top Left) vs. No Defect (Top Right) at 120 μs , with Difference (Bottom)

Figure 4.37 shows the compression wave at 300 μ s, as the compression wave reaches the receiver access tubes. The compression wave reaches the access tubes in both models at essentially the same time.

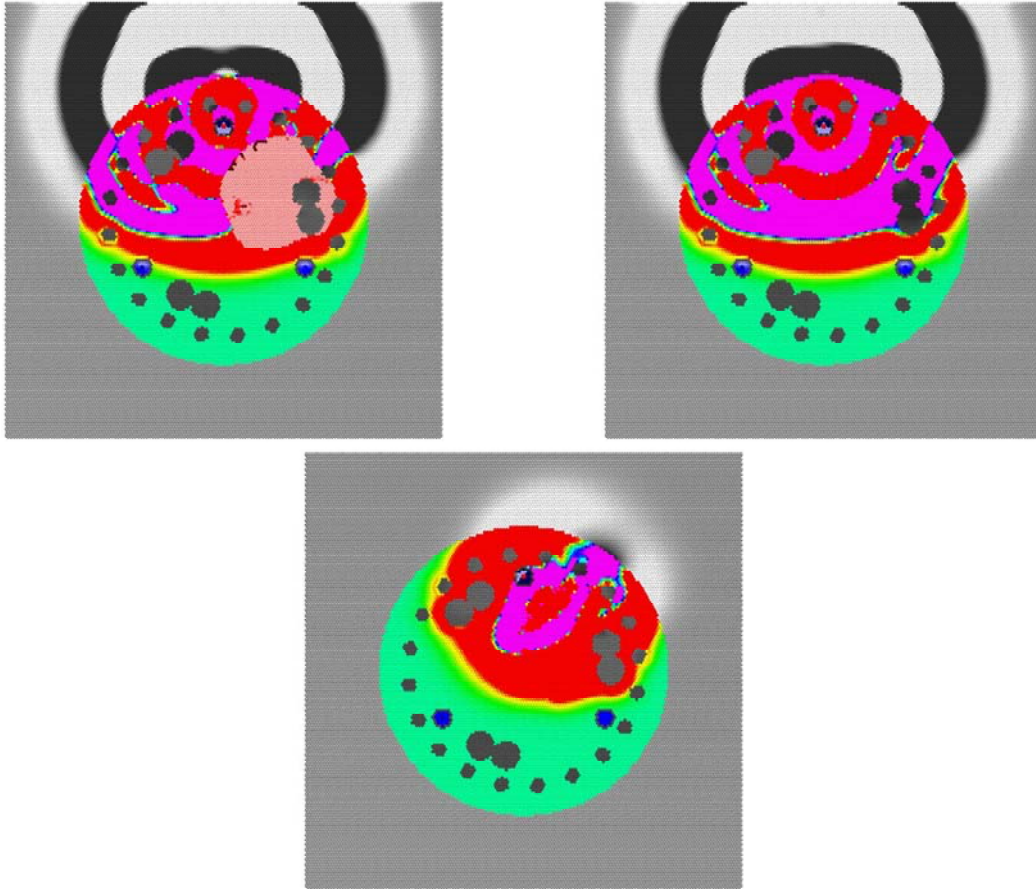


Figure 4.37. Plot. Cracking Defect (Top Left) vs. No Defect (Top Right) at 300 μ s, with Difference (Bottom)

Figure 4.38 shows the compression wave at 500 μ s, as the peak of the first tension wave crosses the access tubes in the shaft with no defect. The tension wave in the shaft with cracking defect is almost non-existent at the access tube.

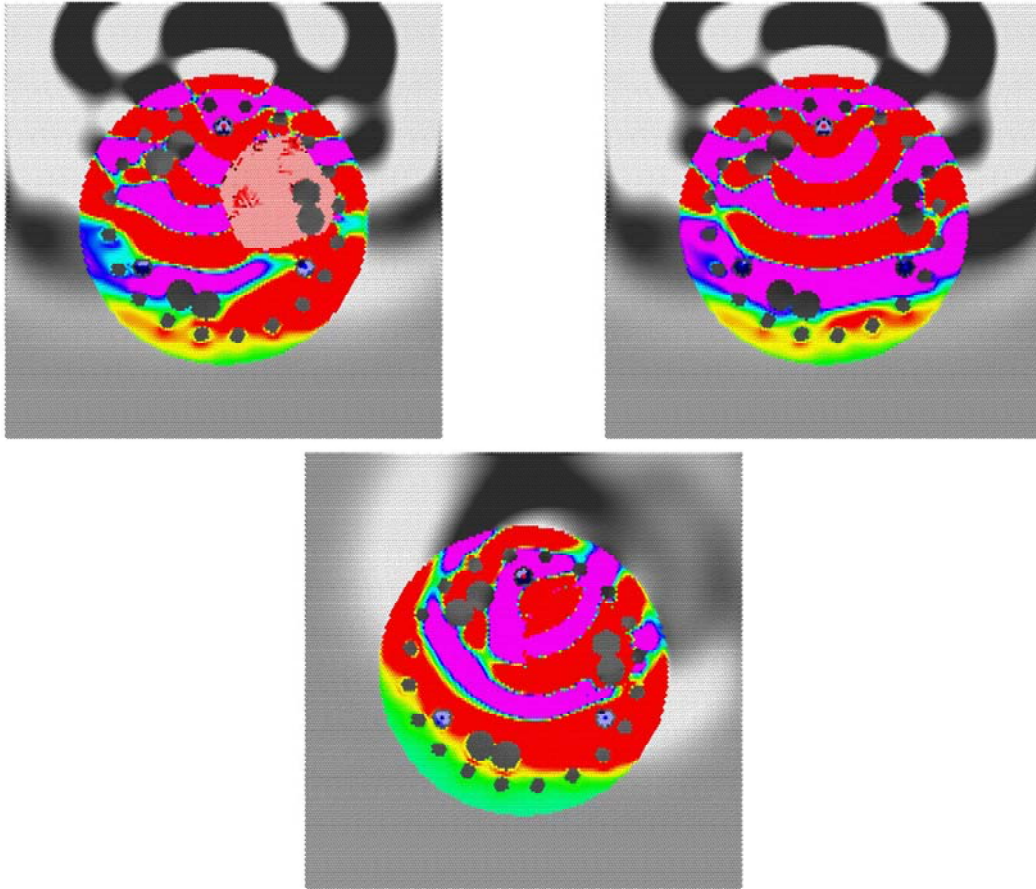


Figure 4.38. Plot. Cracking Defect (Top Left) vs. No Defect (Top Right) at 500 μ s, with Difference (Bottom)

Figure 4.39 compares the waveforms collected in the access tubes. Since the cracking defect is between tubes 1 and 2, the top graph shows a much greater effect in the signal. No tension wave was propagated through the cracking defect.

Cracking does result in a significant difference in the full waveform. However, this difference does not appear in the first arrival portion of the signal, and does not significantly affect signal energy. This confirms the observation that UPV lab tests cannot measure cracking or predict specimen strength, in turn suggesting that CSL surveys will fail to detect these defects as well.

Micro-cracking readily allows propagation of compression waves, but severely attenuates and resists propagation of tension waves. Figure 4.39 shows little effect on the first arrival time, but a significant change in the amplitude of later portions of the signal at the receiver.

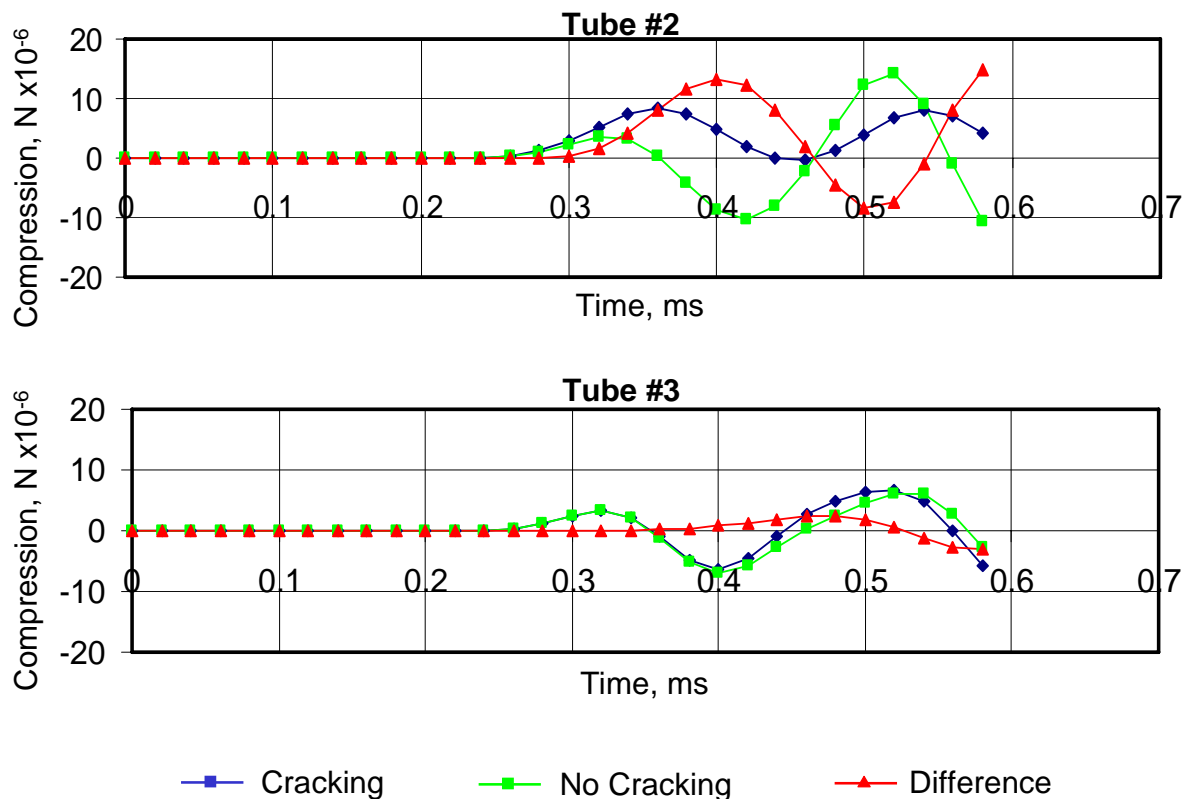


Figure 4.39. Chart. CSL Signals with a Cracking Defect vs. No Defect, between Access Tubes 1 and 2 (Top), and Tubes 1 and 3 (Bottom)

4.7.1 Concrete Strength Reduction

Since by its chemical nature concrete is not as thermodynamically stable as natural stone, concrete is susceptible to various forms of physical and chemical deterioration. A number of different factors can result in concrete deterioration from physical and chemical weathering. Deterioration from sunlight can cause heat-induced surface cracking. Abrasion also can affect surfaces. For large concrete structures, chemical weathering is more significant, as damage can occur deep within the concrete structure.

Various chemical agents in the environment can cause chemical weathering or corrosion due to the reactive nature of cement. Carbon dioxide at normal atmospheric concentrations is the source of carbonic acid, which naturally reacts with and breaks down cement. This process is accelerated by acid rain, which also contains more reactive compounds such as sulfuric acid. Other sources of corrosion include the ingress of sulfates in ground water, which readily attack cement and lead to corrosion.

Reinforcing steel that is encased in concrete is naturally protected from corrosion (i.e. oxidation) because the concrete provides a highly alkaline environment. The pH of concrete including that of the pore solution is about 12.5. At a pH of 11.5 and higher, a passivating oxide film will form on the steel surfaces in contact with the concrete. As long as the passivating oxide film forms, and the high pH environment is maintained, the reinforcing steel will be protected from corrosion.

Concrete surfaces exposed to the atmosphere (CO_2) carbonate (i.e. the pH will be reduced from 12.5 to about 8.5). With time, the carbonation will progress as a front from the exposed surfaces inward toward the reinforcing steel. When the carbonation front reaches reinforcing steel or serves to reduce the pH of the pore solution sufficiently, the rebar will corrode. In concrete of low cover and permeability, this process takes decades. In concrete of high permeability, the process can take a few years.

Corrosion can also initiate in voids that interface with the steel, particularly in instances where the rebar has not been properly encased with concrete and numerous voids exist. At the void-steel interface, the passivating oxide film may have never formed or be very unstable. The voids also harbor water and oxygen, which further fuels corrosion in a low pH environment. Additionally, the chloride ion is attracted to corroding sites. It can be present in the environment surrounding the structure and ingress inward through voids and cracks in the concrete to further destroy the passivating oxide film surrounding the rebar. Wetting (provided by rain or a fluctuating water table) and subsequent drying can replenish and concentrate salts on the concrete surface leading to continual attack and deterioration. Corrosion products are more voluminous (about twice the size) of the original parent material. As they continue to expand, they cause additional cracking and deterioration of the concrete matrix.

Deterioration over time can cause large areas of weakness and cracking in the concrete, lowering bearing capacity below design specifications. The progression of chemical weathering is closely related to a basic chemical defect of concrete: the tendency to crack. The ingress of chemical

agents into concrete is directly proportional to the initial permeability of the concrete, and permeability is directly proportional to cracking. Cracking allows a pathway for corrosive agents of all kinds to penetrate deep within the concrete. Crack prevention is a key factor in improving concrete durability and resistance to deterioration.

The strength and performance of the concrete is dependent on the cracking extent within the structure. Cracking does cause a substantial decrease in both Poisson's Ratio and the stiffness of the concrete. However, cracking does not, in and of itself, necessarily result in major impacts on strength. This is especially true for concrete structures reinforced with rebar. Cracking affects the stability of tensile load behavior of concrete more than any other characteristic, so failure strength is reduced substantially in non-reinforced concrete structures by only moderate levels of cracking. Steel reinforces the tensile strength of the concrete structure so that moderate levels of cracking do not compromise structural capacity in the short term. However, the effects of cracking are a significant issue for long-term stability and durability.

4.8 Honeycombs Effects

Honeycombs are regions in concrete with a high concentration of small void areas, with a small degree of cracking. The grainy consistency in some cases can be compared with common cinder blocks sold in hardware stores. Honeycombs can be formed by using an improper cement mixture, inadequate vibration of the mixture, improper placement, by the presence of oversized aggregate, or by too tight of a spacing of the reinforcement as compared to the maximum aggregate size. For example, a portion of the sidewall of the drilled shaft could fall into the shaft during concrete placement and form a region of honeycombed concrete. The cement volume is inadequate to fill in all the gaps between the aggregate, resulting in a cluster of small voids resembling a honeycomb in appearance. Concrete strength is significantly reduced in areas of concrete affected by honeycombing. Honeycombed defects are modeled by randomly replacing a certain percentage of concrete with a void material and specifying a small percentage of cracking.

Figures 4.40 – 4.45 compare CSL signals from a drilled shaft with a honeycomb defect, shown in red, to a shaft with no defect. The honeycomb defect has slightly slower compression wave velocity, with 10% of the springs broken, and is 20% void.

Figure 4.40 shows the compression wave propagating from the source access tube after 20 μ s.

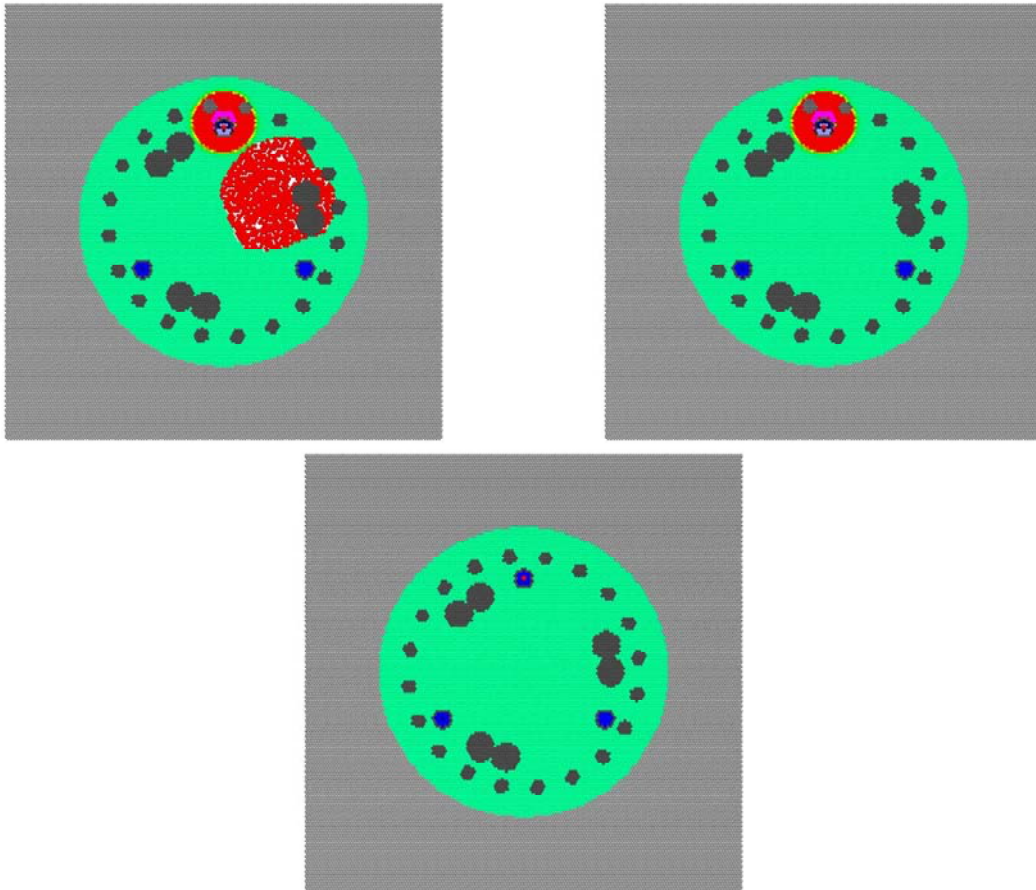


Figure 4.40. Plot. Honeycomb Defect (Top Left) vs. No Defect (Top Right) at 20 μs , with Difference (Bottom)

The wavefront first encounters the honeycomb defect in Figure 4.41 at $60 \mu\text{s}$. The difference plot shows the effect of the honeycomb defect on the compression wave.

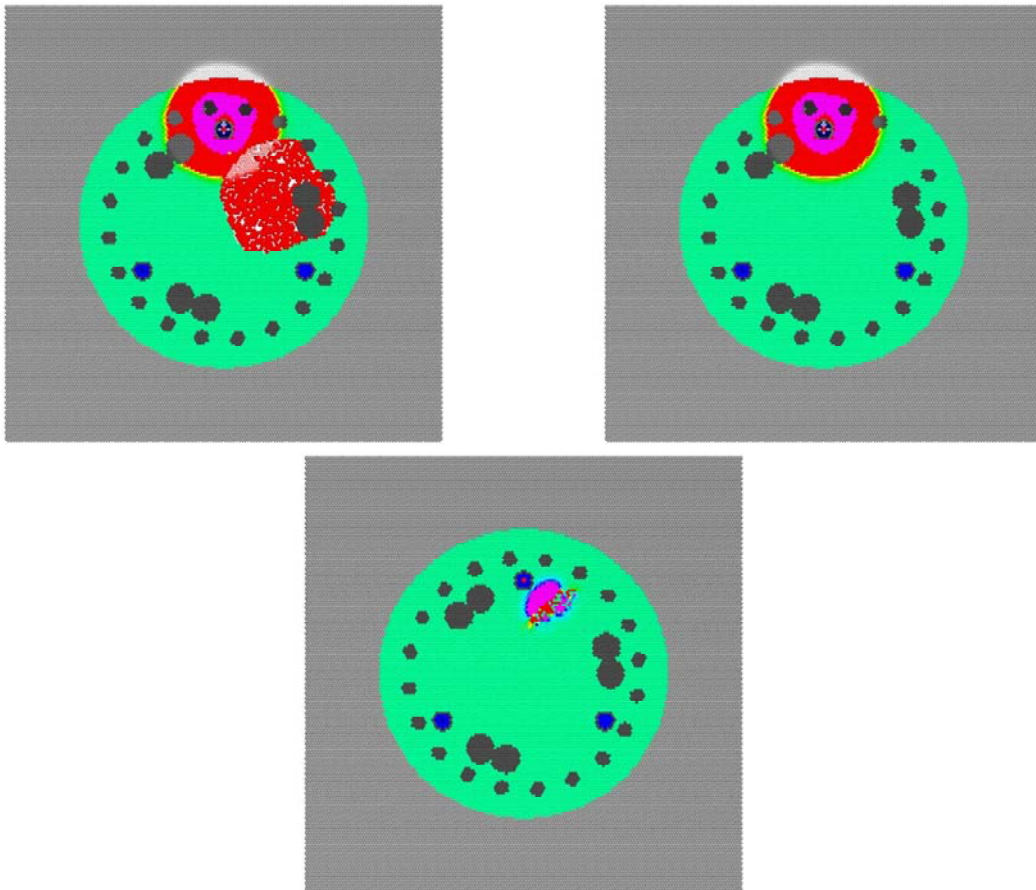


Figure 4.41. Plot. Honeycomb Defect (Top Left) vs. No Defect (Top Right) at $20 \mu\text{s}$, with Difference (Bottom)

Figure 4.42 shows the compression wave at 120 μs , as the compression wave passes half way through the honeycomb defect. The voids inside the honeycomb defect delay and attenuate the wavefront.

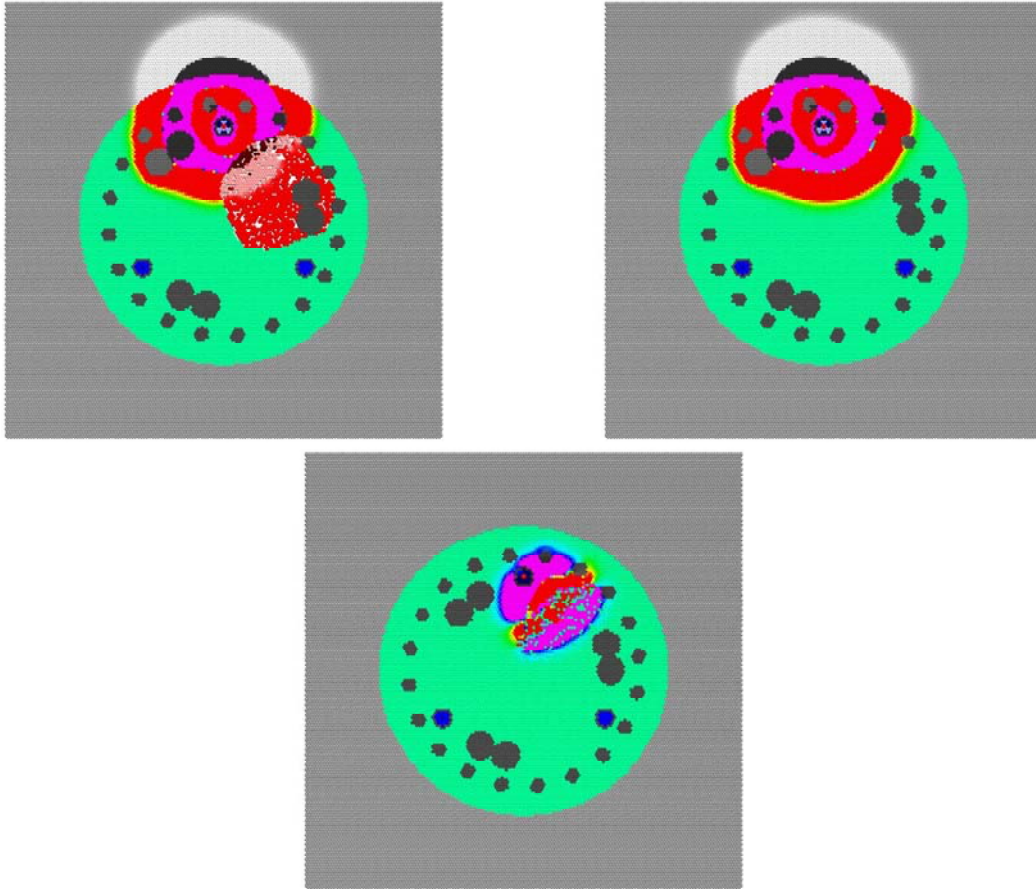


Figure 4.42. Plot. Honeycomb Defect (Top Left) vs. No Defect (Top Right) at 120 μs , with Difference (Bottom)

Figure 4.43 shows the compression wave at $300 \mu\text{s}$, as the compression wave reaches the receiver access tubes in the shaft with no defect. The compression wave is significantly delayed by the honeycomb defect.

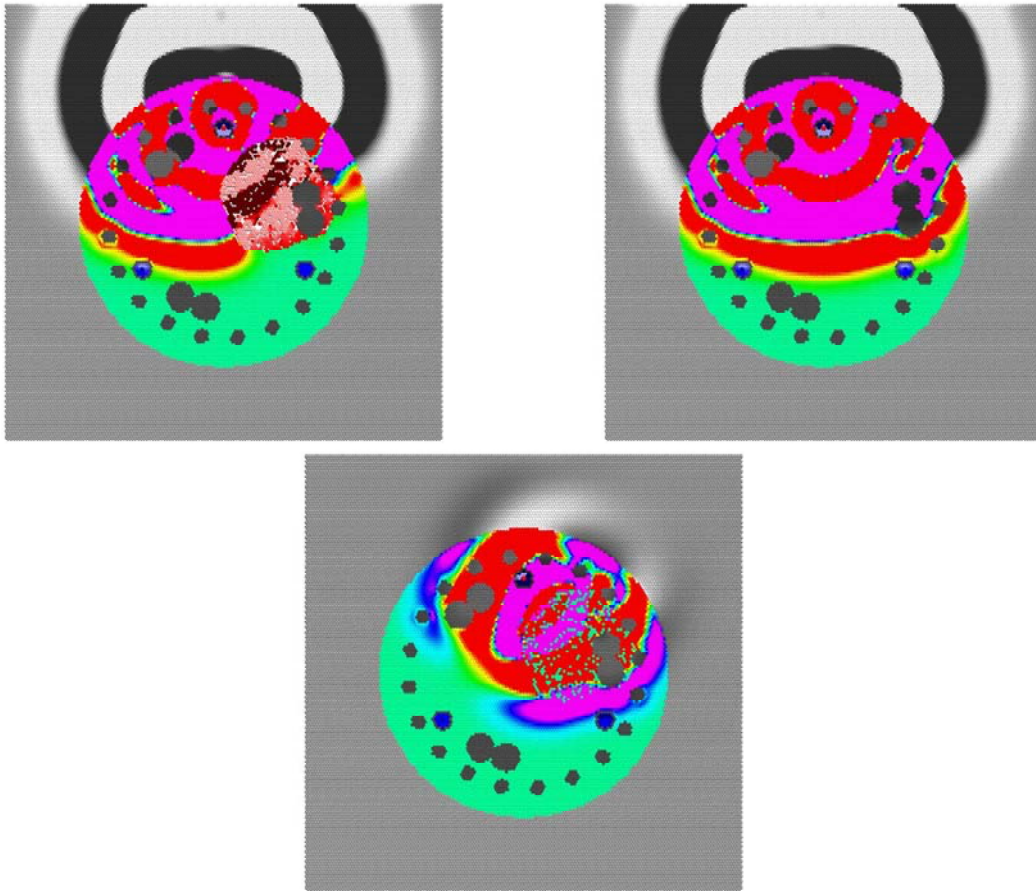


Figure 4.43. Plot. Honeycomb Defect (Top Left) vs. No Defect (Top Right) at $300 \mu\text{s}$, with Difference (Bottom)

Figure 4.44 shows the compression wave at $500 \mu\text{s}$, as the peak of the first tension wave crosses the access tubes in the shaft with no defect. A small attenuated compression wave is crossing tube 2 in the shaft with the honeycomb defect.

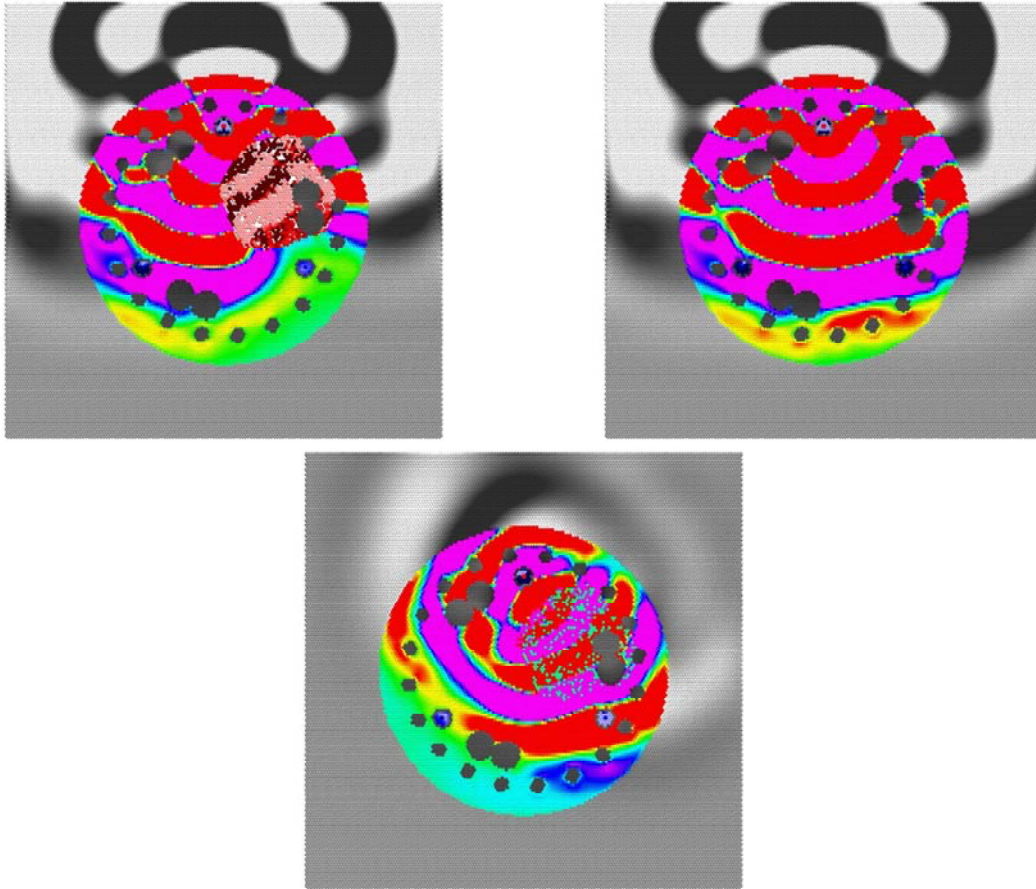


Figure 4.44. Plot. Honeycomb Defect (Top Left) vs. No Defect (Top Right) at $500 \mu\text{s}$, with Difference (Bottom)

Figure 4.45 compares the waveforms collected in the access tubes. The top graph shows that the honeycomb defect almost entirely attenuates the signal between tubes 1 and 2.

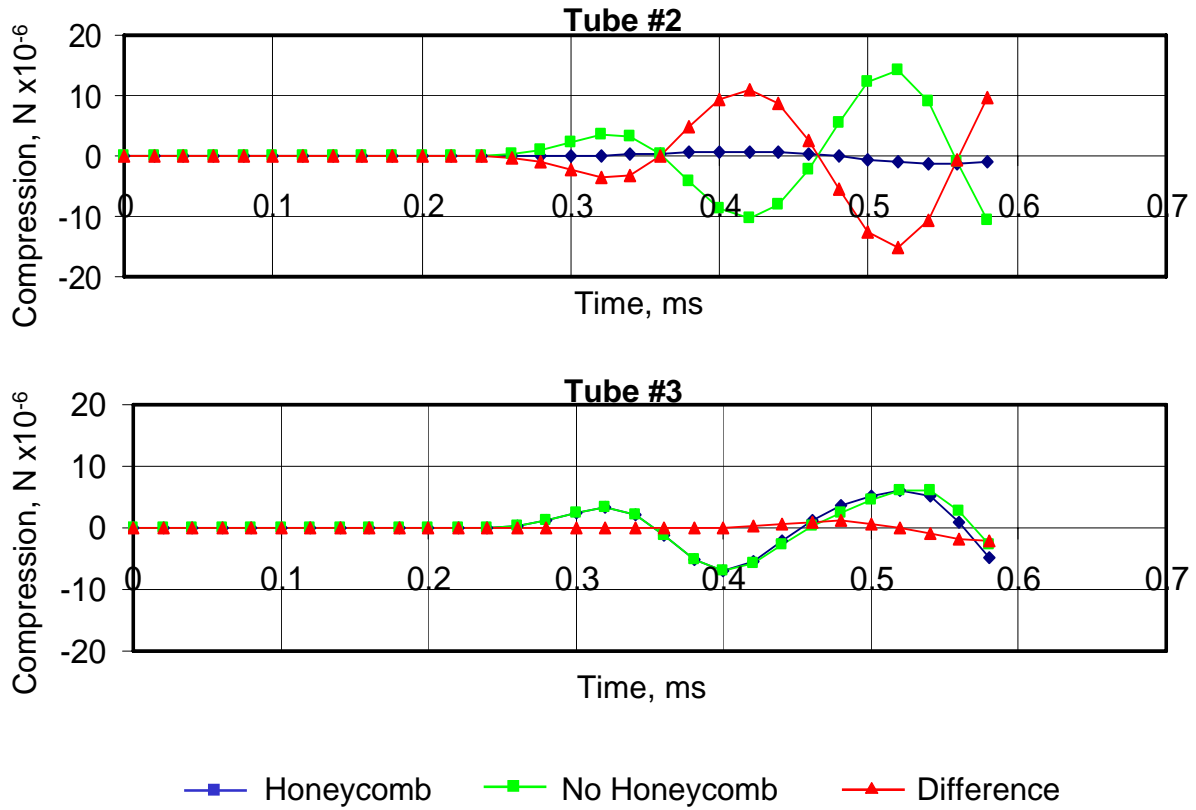


Figure 4.45. Chart. CSL Signals with a Honeycomb Defect vs. No Defect, between Access Tubes 1 and 2 (Top), and Tubes 1 and 3 (Bottom)

4.9 Effect of Voids

Occasionally concrete can be displaced by water or debris, resulting in fluid-filled voids. The voids may be filled with air or water, depending on conditions. Air-filled voids are more easily detected, so a water-filled void will be investigated instead. Figure 4.38 shows the source activation in a shaft with a water-filled void with the same size, shape, and location as the honeycomb and cracking defects previously examined.

Figures 4.46 – 4.51 show the effect of the void on the compression waves. The void is the same size as the cracking and honeycomb defects.

Figure 4.46 shows the compression wave propagating from the source access tube after 20 μs .

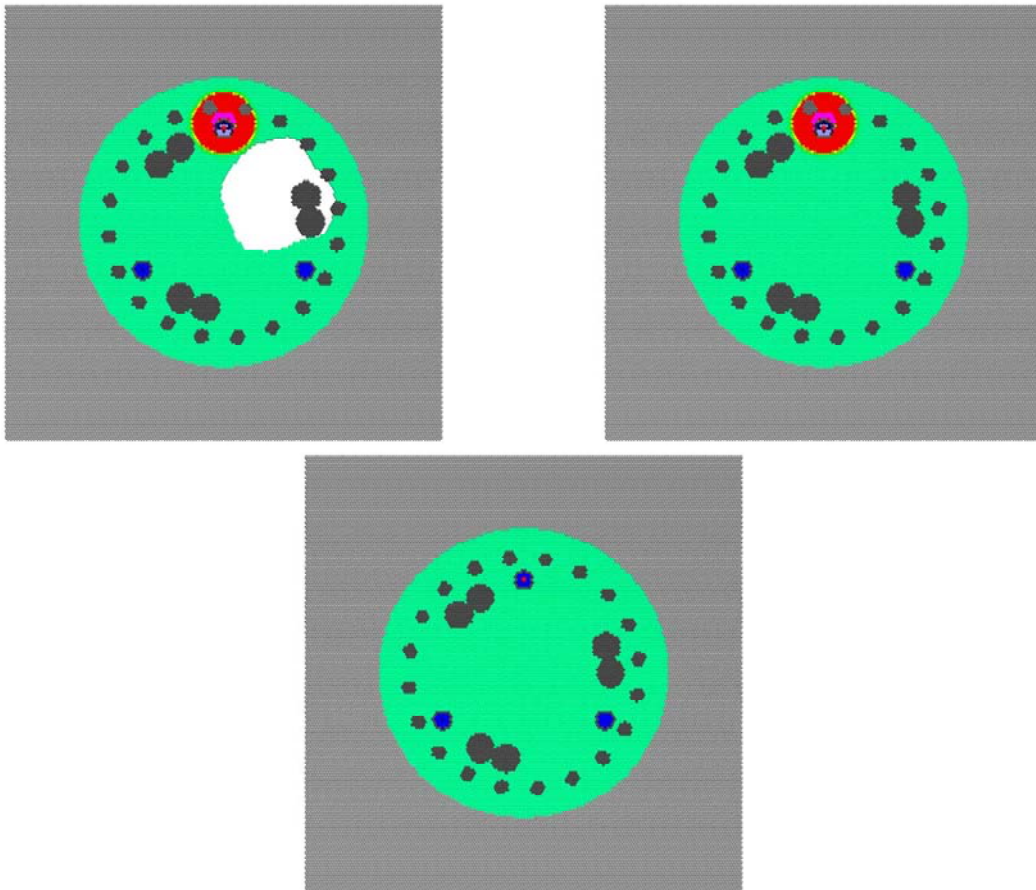


Figure 4.46. Plot. Void Defect (Top Left) vs. No Defect (Top Right) at 20 μs , with Difference (Bottom)

The wavefront first encounters the void in Figure 4.47 at $60 \mu\text{s}$. The difference plot shows the reflection of the compression wave from the void.

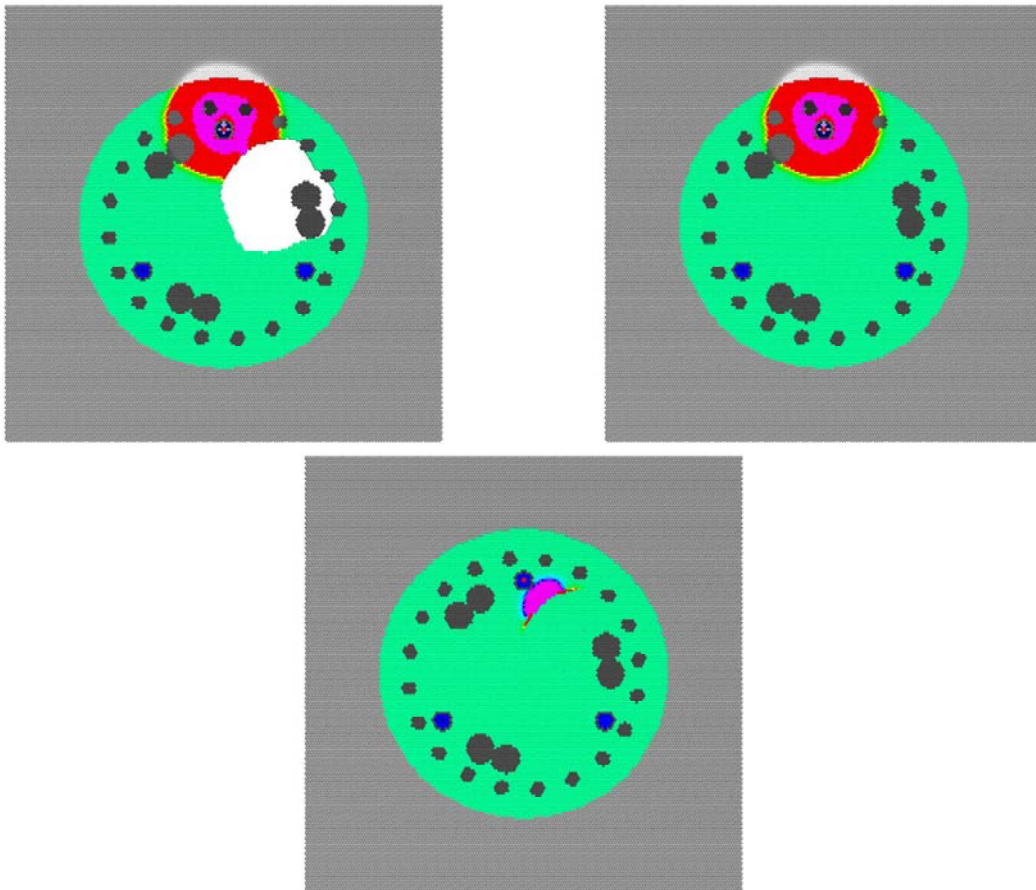


Figure 4.47. Plot. Void Defect (Top Left) vs. No Defect (Top Right) at $20 \mu\text{s}$, with Difference (Bottom)

Figure 4.48 shows the compression wave at 120 μs , as the compression wave passes half way around the void.

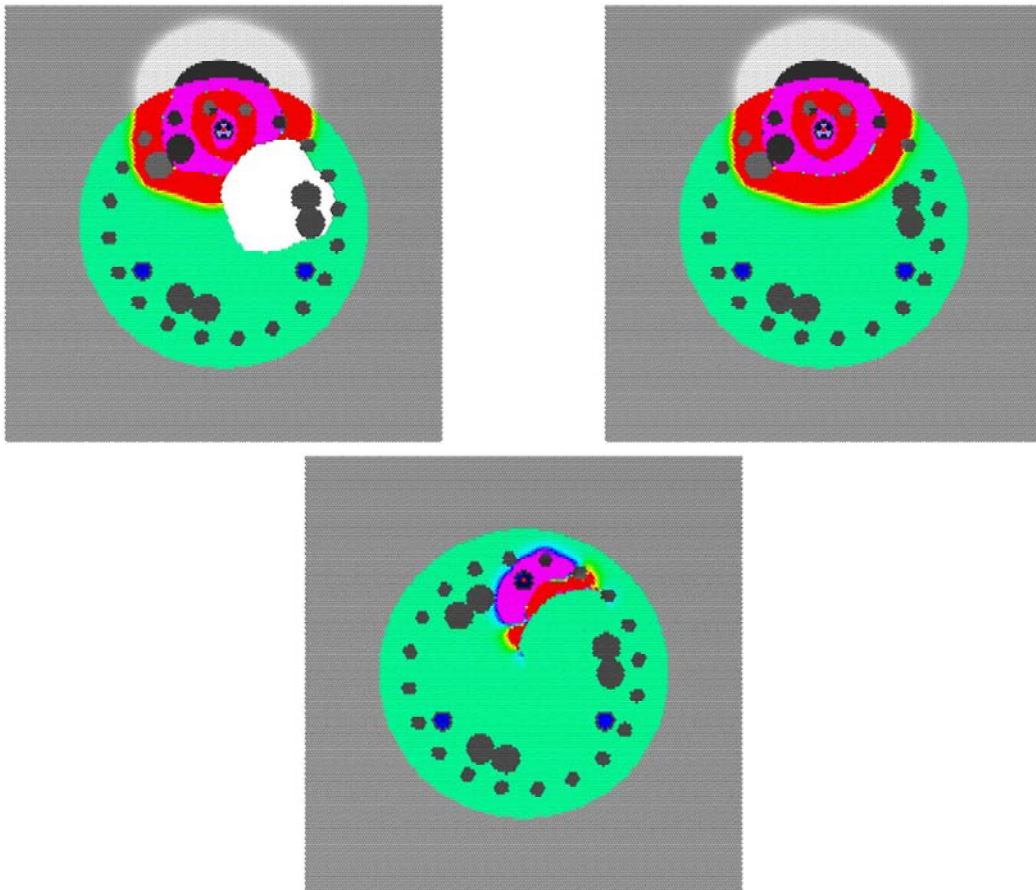


Figure 4.48. Plot. Void Defect (Top Left) vs. No Defect (Top Right) at 120 μs , with Difference (Bottom)

Figure 4.49 shows the compression wave at 300 μs , as the compression wave reaches the receiver access tubes in the shaft with no void. The compression wave has not quite encircled the void.

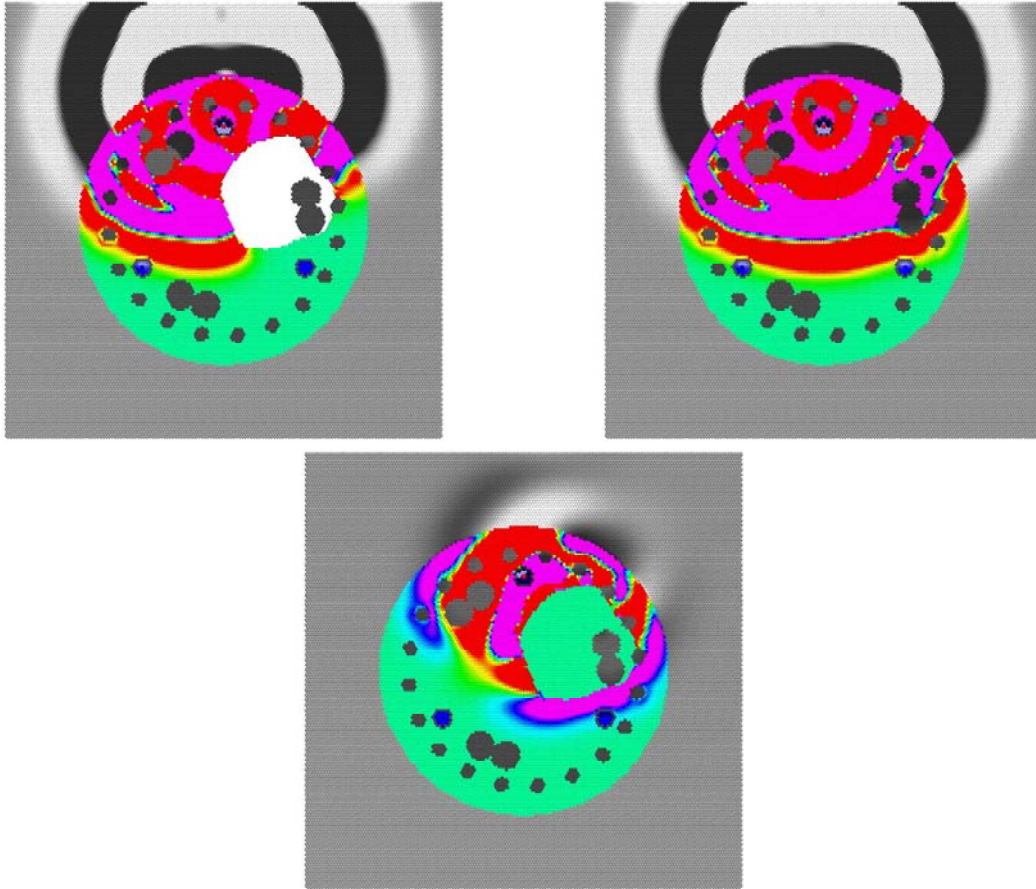


Figure 4.49. Plot. Void Defect (Top Left) vs. No Defect (Top Right) at 300 μs , with Difference (Bottom)

Figure 4.50 shows the compression wave at $500 \mu\text{s}$, as the peak of the first tension wave crosses the access tubes in the shaft with no void. The void has almost completely attenuated the first compression wave.

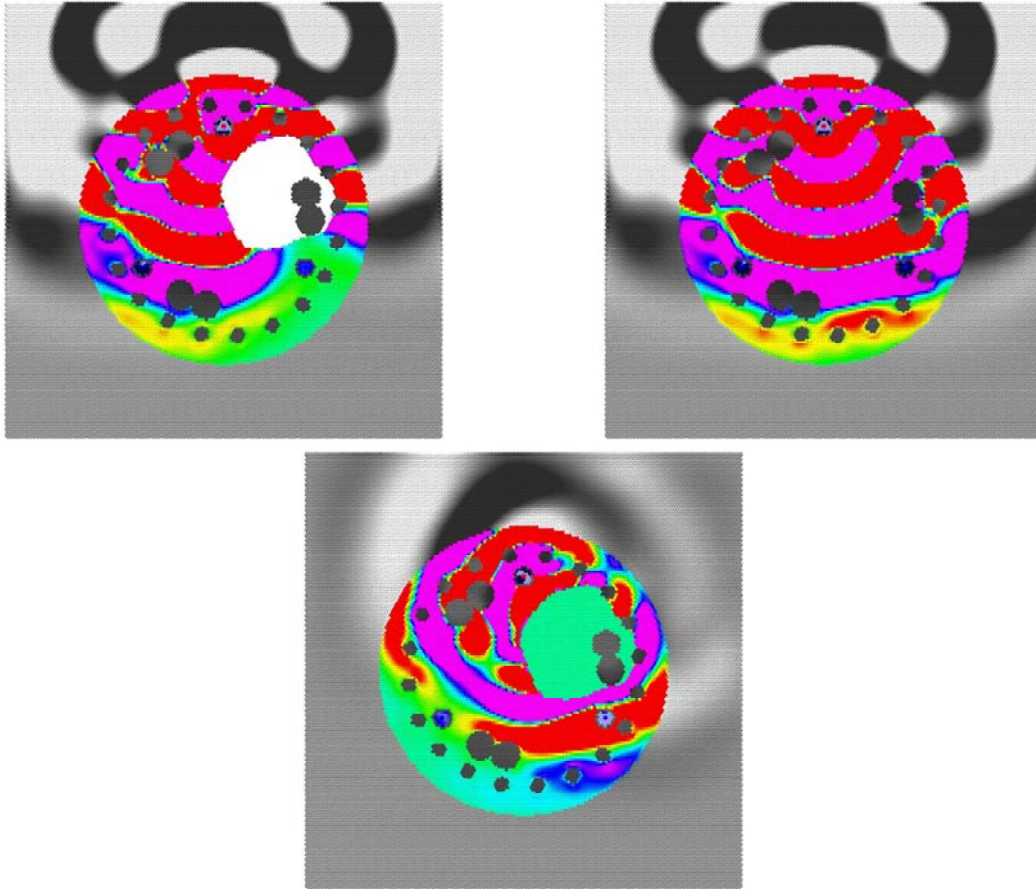


Figure 4.50. Plot. Void Defect (Top Left) vs. No Defect (Top Right) at $500 \mu\text{s}$, with Difference (Bottom)

Figure 4.51 compares the waveforms collected in the access tubes. The void significantly blocks the signal between tubes 1 and 2.

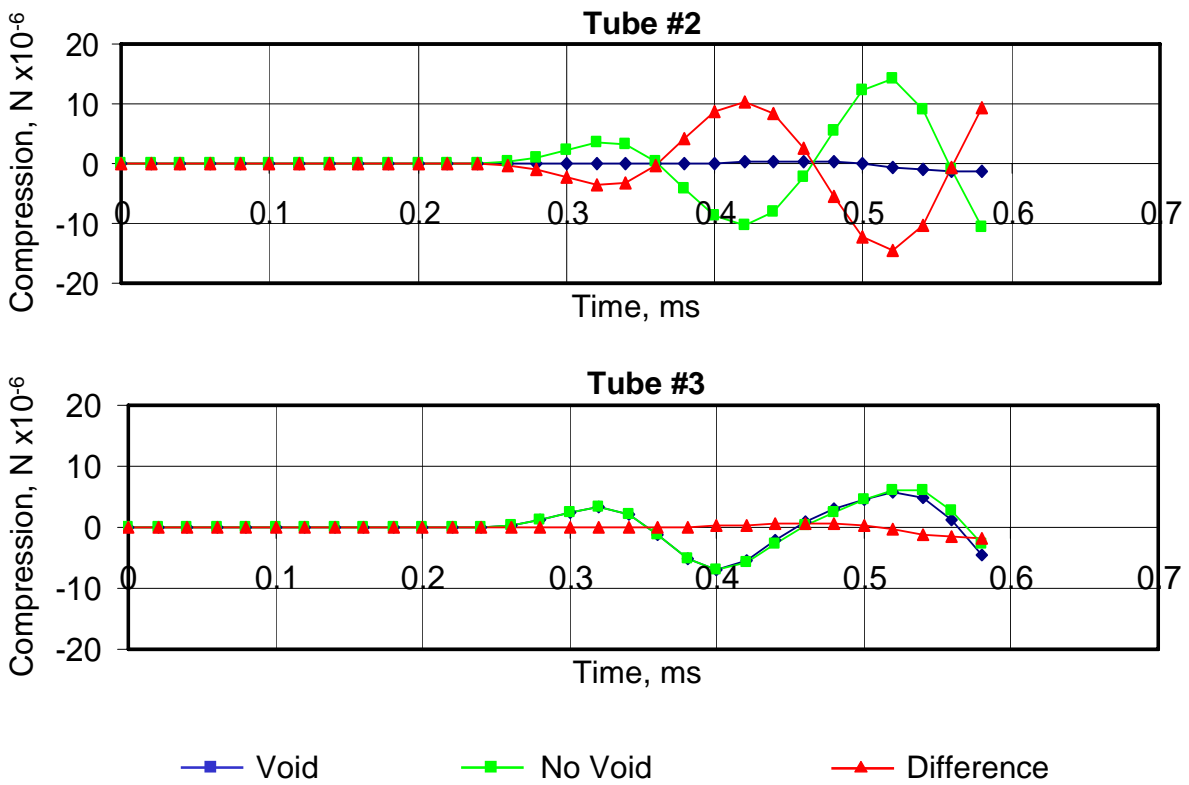


Figure 4.51. Chart. CSL Signals with a Void vs. No Defect, between Access Tubes 1 and 2 (Top), and Tubes 1 and 3 (Bottom)